

Connexin 30 sets synaptic strength by controlling astroglial synapse invasion

Ulrike Pannasch^{1,2,10}, Dominik Freche^{3,4,11}, Glenn Dallérac^{1,2,11}, Grégory Ghézali^{1,2}, Carole Escartin⁵, Pascal Ezan^{1,2}, Martine Cohen-Salmon^{1,2}, Karim Benchenane⁶, Veronica Abudara^{1,2,10}, Amandine Dufour⁷, Joachim H R Lübke^{7,8}, Nicole Déglon^{5,10}, Graham Knott⁹, David Holcman^{3,4} & Nathalie Rouach^{1,2}

Astrocytes play active roles in brain physiology by dynamic interactions with neurons. Connexin 30, one of the two main astroglial gap-junction subunits, is thought to be involved in behavioral and basic cognitive processes. However, the underlying cellular and molecular mechanisms are unknown. We show here in mice that connexin 30 controls hippocampal excitatory synaptic transmission through modulation of astroglial glutamate transport, which directly alters synaptic glutamate levels. Unexpectedly, we found that connexin 30 regulated cell adhesion and migration and that connexin 30 modulation of glutamate transport, occurring independently of its channel function, was mediated by morphological changes controlling insertion of astroglial processes into synaptic clefts. By setting excitatory synaptic strength, connexin 30 plays an important role in long-term synaptic plasticity and in hippocampus-based contextual memory. Taken together, these results establish connexin 30 as a critical regulator of synaptic strength by controlling the synaptic location of astroglial processes.

Bidirectional communication between astrocytes and neurons has recently been shown to regulate neuronal excitability, synaptic transmission and plasticity¹. Indeed, astrocytes are dynamic signaling brain elements that sense neuronal inputs by their ion channels, neurotransmitter receptors and transporters, and can respond by complex calcium signaling, morphological plasticity and uptake or release of numerous neuroactive factors to modulate neighboring pre- and postsynaptic elements^{2–4}. However, the detailed molecular mechanisms of such regulations are still elusive.

A key property of astrocytes is the expression of high levels of the gap junction proteins connexins (Cx) 30 and 43, thought to contribute to brain homeostasis through their role in intercellular communication, mediating nutrient transport and potassium buffering⁵. Recent studies also indicate that connexin functions extend beyond the classic intercellular communication and include hemichannel-mediated exchange with the extracellular space, as well as channel-independent functions involving protein interactions, cell adhesion and intracellular signaling^{6,7}. Although Cx43 is already established as a key player in brain development and physiology^{5,6}, the role of Cx30, expressed in astrocytes later during development—after postnatal day (P) 10 (ref. 8)—has been unexplored. Because astroglial Cx43 and Cx30 show differential temporal and spatial distributions⁸, biophysical properties⁹,

C-terminal domains, regulation by neuronal activity¹⁰ and contributions to behavior^{11–13}, determining the specific role of Cx30 on neuronal physiology is a key issue. Notably, Cx30 is thought to be involved in behavioral and basic cognitive processes, as it is upregulated in mice raised in enriched environments¹⁴, known to promote structural changes in the brain and to enhance learning and memory performance, and its elimination alters the reactivity of mice to novel environments and object recognition memory¹¹.

To understand the cellular and molecular basis of Cx30 regulation of neuronal information processing, we investigated the specific role of Cx30 in hippocampal synaptic transmission, plasticity and memory. Mice deficient in Cx30 protein showed decreased excitatory synaptic transmission mediated by AMPA receptors (AMPA) and impaired synaptic plasticity through modulation of synaptic glutamate levels. This effect was due to altered astroglial glutamate clearance resulting from changes in astrocytic morphology, controlling astroglial processes insertion into synaptic clefts. We furthermore identified Cx30 as a critical regulator of cellular adhesion and migration, and found that the modulation of astroglial morphology and synaptic transmission involved an unconventional, non-channel function of Cx30. Strikingly, Cx30 regulation of synaptic efficacy altered hippocampus-based contextual memory. Altogether, this establishes Cx30 as a key

¹Center for Interdisciplinary Research in Biology, Collège de France, INSERM U1050, CNRS UMR 7241, Labex Memolife, PSL Research University, Paris, France.

²Doctoral school N° 158, Pierre and Marie Curie University, Paris, France. ³Institute of Biology, Ecole Normale Supérieure, INSERM 1024, CNRS UMR 8197, Paris, France. ⁴Department of Mathematics, Weizmann Institute of Science, Rehovot, Israel. ⁵CNRS URA2210, Commissariat à l'Energie Atomique et aux Energies Alternatives, MIRCen, Fontenay-aux-Roses, France. ⁶CNRS UMR 7637, Ecole Supérieure de Physique et de Chimie Industrielles, Paris, France. ⁷Institute for Neuroscience and Medicine INM-2, Research Center Jülich, Jülich, Germany. ⁸Department of Psychiatry, Psychotherapy and Psychosomatics, Rheinisch-Westfälische Technische Hochschule Aachen University, Jülich-Aachen Research Alliance Translational Brain Medicine, Aachen, Germany. ⁹Center of Interdisciplinary Electron Microscopy, École polytechnique fédérale de Lausanne, Lausanne, Switzerland. ¹⁰Present addresses: Neuroscience Research Center, Charité-Universitätsmedizin, Berlin, Germany (U.P.); Departamento de Fisiología, Facultad de Medicina, Universidad de la República, Montevideo, Uruguay (V.A.); Department of Clinical Neurosciences, Lausanne University Hospital, Lausanne, Switzerland (N.D.). ¹¹These authors contributed equally to this work. Correspondence should be addressed to N.R. (nathalie.rouach@college-de-france.fr).

Received 4 November 2013; accepted 27 January 2014; published online 2 March 2014; doi:10.1038/nn.3662

molecular determinant of astroglial synapse coverage, controlling synaptic strength and memory.

RESULTS

Cx30 regulates hippocampal excitatory synaptic strength

To examine the contribution of Cx30 to synaptic strength, we first evaluated basal evoked synaptic transmission at CA1 Schaffer collateral synapses in acute hippocampal slices from *Cx30*^{-/-} (also known as *Gjb6*^{-/-}) mice. We found a ~35% reduction in synaptic transmission in *Cx30*^{-/-} mice by comparing the amplitude of the presynaptic fiber volley (input) to the slope of the field excitatory postsynaptic potential (fEPSP) (output) (Fig. 1a). As fEPSPs are largely mediated

by AMPA receptors (AMPA), we tested for changes in membrane AMPAR density, by recording in the presence of tetrodotoxin whole-cell responses of pyramidal cells to local application of AMPA, which activates synaptic and extrasynaptic AMPARs throughout the cell. The size of the evoked current was similar in *Cx30*^{-/-} and *Cx30*^{+/+} mice (Fig. 1b). In addition, normalization of the current to membrane capacitance, unchanged in CA1 pyramidal cells from *Cx30*^{-/-} mice (*Cx30*^{+/+}, 136 ± 8 pF, *n* = 58 cells; *Cx30*^{-/-}, 132 ± 10 pF, *n* = 28 cells, *P* = 0.7923, *U* = 783, Mann-Whitney), gave similar results (*Cx30*^{+/+}, 4.39 ± 0.53, *n* = 12 cells; *Cx30*^{-/-}, 4.43 ± 0.51, *n* = 10 cells, *P* = 0.6194, *U* = 52, Mann-Whitney), suggesting no change in surface AMPAR density. We then determined whether the reduction in

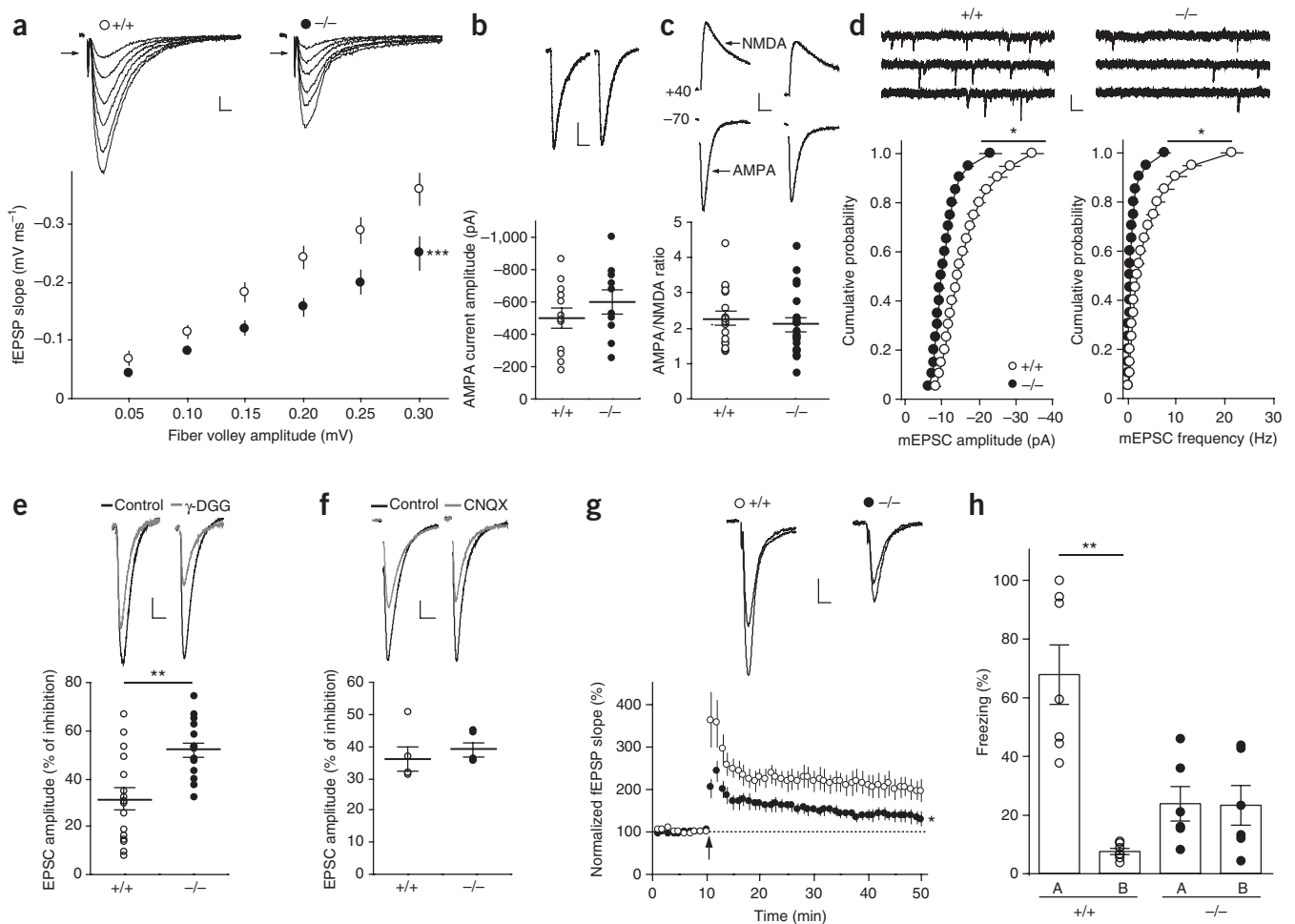


Figure 1 Cx30 controls synaptic strength by regulating synaptic glutamate levels. **(a)** Input-output curves for basal synaptic transmission, illustrated in the sample traces and the graph below. fEPSP slope (output) was decreased in *Cx30*^{-/-} mice (input, arrow) (*Cx30*^{+/+} *n* = 25 slices, *Cx30*^{-/-} *n* = 24 slices; genotype: *P* < 0.0001, *F*(1,282) = 41.03; fiber volley: *P* < 0.0001, *F*(5,282) = 52.05; two-way ANOVA). Scale bar, 0.1 mV and 5 ms. **(b)** Whole-cell evoked AMPAR currents (5 s, 10 μ M AMPA + 100 μ M cyclothiazide + 0.5 μ M TTX) in pyramidal cells from *Cx30*^{+/+} (*n* = 12 cells) and *Cx30*^{-/-} mice (*n* = 10 cells) were similar (*P* = 0.2897, *t*(20) = 1.088, unpaired *t* test). Scale bar, 50 pA and 20 s. **(c)** Ratios of AMPA to NMDA EPSCs in pyramidal cells from *Cx30*^{+/+} (*n* = 17 cells) and *Cx30*^{-/-} mice (*n* = 22 cells) were similar (*P* = 0.4561, *t*(37) = 0.7531, unpaired *t* test). Scale bar, 20 pA and 20 ms. **(d)** Cumulative distributions of mEPSC amplitude and frequency, with sample traces above, differed between *Cx30*^{-/-} (*n* = 8 cells) and *Cx30*^{+/+} mice (*n* = 8 cells) (mEPSC amplitude: *P* = 0.0348, *KS* = 0.45; mEPSC frequency: *P* = 0.0348, *KS* = 0.45; Kolmogorov-Smirnov). Scale bar, 10 pA and 250 ms. **(e)** Synaptic glutamate levels, revealed by γ -DGG (0.5 mM) inhibition of EPSC amplitude (gray trace), were reduced in *Cx30*^{-/-} mice (*Cx30*^{+/+} *n* = 16 cells, *Cx30*^{-/-} *n* = 15 cells, *P* = 0.0013, *t*(15) = 3.947, unpaired *t* test). Scale bar, 10 pA and 20 ms. **(f)** Inhibition of the EPSC amplitude by CNQX (0.5 μ M, gray trace) in *Cx30*^{-/-} (*n* = 5 cells) and *Cx30*^{+/+} mice (*n* = 5 cells) was similar (*P* = 0.4127, *U* = 8, Mann-Whitney). Scale bar, *Cx30*^{+/+} 20 pA, *Cx30*^{-/-} 15 pA, and 20 ms. **(g)** Tetanus-induced LTP (arrow, two 100 Hz tetani for 1 s, interval 20 s) was reduced in *Cx30*^{-/-} (*n* = 7 slices) as compared to *Cx30*^{+/+} slices (*n* = 8 slices, *P* = 0.0423, *t*(13) = 2.252, comparison 30–40 min after the tetanus, unpaired *t* test). Sample traces represent averaged fEPSPs before and 30–40 min after tetanization. Scale bar, 0.1 mV and 10 ms. **(h)** In *Cx30*^{-/-} mice, fear conditioning was unable to induce enhanced freezing behavior in response to the conditioning context A, unlike in *Cx30*^{+/+} mice. (*Cx30*^{+/+} *n* = 7 mice, *P* = 0.002, *U* = 0; *Cx30*^{-/-} *n* = 6 mice, *P* = 0.81, *U* = 16, Mann-Whitney). All data are expressed as mean \pm s.e.m. **P* < 0.05, ***P* < 0.01, ****P* < 0.001.

excitatory synaptic transmission was specific to AMPARs, by comparing the AMPAR and NMDAR components of the EPSC in CA1 pyramidal cells. The AMPA/NMDA ratio was unchanged in *Cx30*^{-/-} mice (Fig. 1c), indicating that the defect in synaptic transmission also affects NMDAR currents. Analysis of AMPAR miniature excitatory postsynaptic currents (mEPSCs) also revealed in *Cx30*^{-/-} mice a reduction in frequency (*Cx30*^{+/+}, 0.99 ± 0.13 Hz, $n = 8$ cells; *Cx30*^{-/-}, 0.49 ± 0.12 Hz, $n = 8$ cells; $P = 0.0122$, $t(14) = 2.875$, unpaired t test) and amplitude (*Cx30*^{+/+}, -14.7 ± 0.5 pA, $n = 8$ cells; *Cx30*^{-/-}, -11.5 ± 0.7 pA, $n = 8$ cells; $P = 0.019$, $t(14) = 3.806$, unpaired t test) of these events (Fig. 1d). Because the cumulative probability showed an overall decrease in mEPSC amplitudes (Fig. 1d), suggesting reduced synaptic glutamate levels, the strong decrease in mEPSC frequency could be secondary to decreased amplitudes of a large subset (~50%) of miniature events below the threshold of detection. Consistent with this hypothesis, partial inhibition of AMPARs with 100 nM CNQX in slices from *Cx30*^{+/+} mice mimicked the decrease in mEPSC frequency and amplitude in *Cx30*^{-/-} mice (Supplementary Fig. 1a). To directly test for a change in synaptic glutamate levels in *Cx30*^{-/-} mice, we used γ -D-glutamylglycine (γ -DGG), a low-affinity competitive antagonist of AMPARs, at a nonsaturating concentration (0.5 mM) at which its potency depends on glutamate concentration. γ -DGG inhibition of evoked AMPAR EPSCs was stronger in pyramidal cells from *Cx30*^{-/-} mice than from *Cx30*^{+/+} mice (Fig. 1e). In contrast, the high-affinity competitive AMPAR antagonist CNQX, used at nonsaturating concentration (500 nM), was similarly effective in pyramidal cells from *Cx30*^{-/-} mice and *Cx30*^{+/+} mice (Fig. 1f). Taken together, these data show that the decreased excitatory synaptic transmission in *Cx30*^{-/-} mice is due to reduced synaptic glutamate, rather than to postsynaptic defects.

To investigate whether in pyramidal cells the defect in synaptic transmission was restricted to excitatory postsynaptic currents, we analyzed miniature inhibitory postsynaptic currents. However we found no significant alteration in their frequency or amplitude in pyramidal cells from *Cx30*^{-/-} mice (Supplementary Fig. 1b).

The alteration of excitatory synaptic activity in pyramidal cells did not result from a developmental defect, as *Cx30* is only expressed after P10 in astrocytes⁸, and before its expression onset, excitatory synaptic transmission, assessed by mEPSCs in P8–P10 mice, was normal in pyramidal cells from *Cx30*^{-/-} mice (Supplementary Fig. 1c). In addition, mice deficient in *Cx30* at later stages showed no gross anatomical defects and presented normal hippocampal architecture and numbers of CA1 pyramidal cells and astrocytes, assessed by NeuN and S100 staining, respectively (Supplementary Fig. 2a,b). Finally, synapse density in stratum radiatum (Supplementary Fig. 2c) and postsynaptic density (PSD) areas (Supplementary Fig. 2d), measured by electron microscopy, as well as levels (Supplementary Fig. 2e) and distributions (data not shown) of the pre- and postsynaptic proteins synaptophysin and PSD-95, were also unchanged in these mice.

Cx30 controls long-term synaptic plasticity and memory

Because *Cx30* regulates synaptic glutamate levels at Schaffer collateral synapses, we investigated its involvement in long-term synaptic plasticity thought to underlie learning and memory. We found that long-term potentiation (LTP), induced by brief tetanic stimulation of Schaffer collaterals, was reduced by ~60% in *Cx30*^{-/-} mice (Fig. 1g). The reduced LTP magnitude arose from weaker NMDAR activation during induction, because pairing of synaptic stimulation with postsynaptic depolarization restored normal LTP in *Cx30*^{-/-} mice (Supplementary Fig. 3a).

Previous studies have shown that hippocampal plasticity is important for contextual learning¹⁵. We thus examined freezing behavior after fear

conditioning sessions in *Cx30*^{-/-} mice and found a strong reduction in contextual fear memory 24 h after conditioning (Fig. 1h).

Cx30 does not alter cell excitability and gliotransmission

How does *Cx30* regulate synaptic glutamate? Schaffer collateral afferent responses were unchanged in *Cx30*^{-/-} mice, as similar stimulation current intensities evoked presynaptic fiber volleys of similar amplitudes in *Cx30*^{-/-} mice and *Cx30*^{+/+} mice (Supplementary Fig. 3b). Intrinsic membrane properties and neuronal excitability were also unchanged in CA1 pyramidal cells from *Cx30*^{-/-} mice, presenting normal resting membrane potentials, action potentials and firing patterns (Supplementary Fig. 3c,d).

Because astrocytes can regulate excitatory transmission through release of gliotransmitters (ATP, glutamate, D-serine)¹, we examined whether these pathways were altered in *Cx30*^{-/-} mice by inhibiting the targeted neuronal receptors. However inhibition of adenosine A1 receptors (A1Rs), NMDARs or metabotropic glutamate receptors (mGluRs) had no differential effect on evoked glutamatergic transmission of pyramidal cells from *Cx30*^{+/+} and *Cx30*^{-/-} mice (Supplementary Fig. 3e). Thus, NMDARs, A1Rs and mGluRs, regulators of presynaptic release, are not involved in the control of synaptic glutamate by *Cx30*.

Cx30 controls excitatory transmission via glutamate uptake

Astrocytes provide the main uptake system for glutamate¹⁶. To investigate whether reduced synaptic glutamate levels in *Cx30*^{-/-} mice are attributable to increased astroglial glutamate clearance, we simultaneously measured synaptically activated glutamate transporter (GLT) currents in astrocytes and neuronal responses (fEPSPs) (Supplementary Fig. 4a). Evoked responses in *Cx30*^{+/+} and *Cx30*^{-/-} hippocampal slices were induced by similar Schaffer collateral stimulation intensity, as assessed by similar fiber volley amplitudes from fEPSPs and evoked potassium currents in astrocytes (Supplementary Fig. 4b,c). However, in *Cx30*^{-/-} mice, the amplitude of astroglial GLT currents, isolated pharmacologically (Supplementary Fig. 4a), was almost doubled (Supplementary Fig. 4d), while the associated excitatory synaptic transmission was decreased (Supplementary Fig. 4e). Consequently, when normalized to the fEPSP slope, the GLT current was increased by ~200% in *Cx30*^{-/-} mice (Fig. 2a). This alteration did not result from changes in intrinsic membrane properties or current profiles of astrocytes in *Cx30*^{-/-} mice (Supplementary Fig. 4f,g).

If increased astroglial glutamate transport is indeed reducing synaptic transmission in *Cx30*^{-/-} mice, reduction of astroglial GLT currents in *Cx30*^{-/-} mice to wild-type levels (by ~50%) should restore normal synaptic transmission. GLT1 inhibition by dihydrokainic acid (DHK, 100 μ M) reduced astroglial transporter currents by ~50% in *Cx30*^{-/-} mice ($-44 \pm 2.4\%$, $n = 4$ cells, $P = 0.0126$, $t(3) = 5.37059$, paired t test), and enhanced synaptic glutamate concentration in *Cx30*^{-/-} mice (Fig. 2b) to wild-type levels (Fig. 1e). DHK also increased the frequency of mEPSCs (Fig. 2c) and the amplitude of evoked EPSCs (Fig. 2d) selectively in CA1 pyramidal cells from *Cx30*^{-/-} mice but not from *Cx30*^{+/+} mice. Finally wild-type LTP magnitude was fully restored in *Cx30*^{-/-} mice by DHK, applied transiently for 3 min before the tetanus (Fig. 2e). Taken together, these results demonstrate that increased glutamate clearance by *Cx30*^{-/-} astrocytes decreases synaptic glutamate concentration and thereby reduces synaptic strength.

Cx30 does not change total glutamate transporter levels

Enhanced astroglial glutamate uptake activity might result from increased GLT expression. However, quantitative western blot analysis

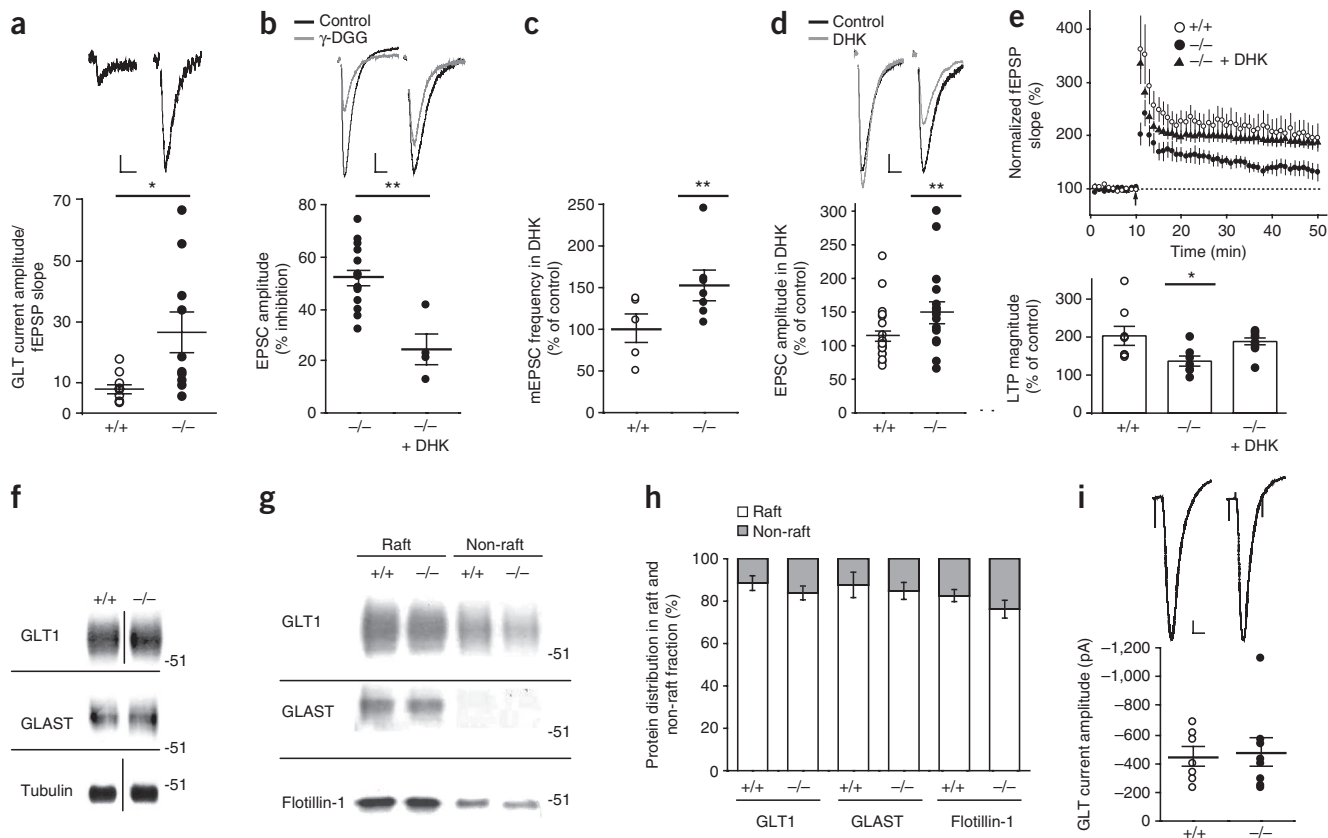


Figure 2 Cx30 control of synaptic glutamate levels is caused by altered astroglial glutamate uptake. **(a)** $Cx30^{-/-}$ astrocytes ($n = 10$ cells) showed greater GLT currents normalized to fEPSP slope than $Cx30^{+/+}$ ($n = 10$ cells, $P = 0.0218$, $t(9.901) = 2.718$, unpaired t test with Welch's correction). Scale bar, 2 pA and 20 ms. **(b–e)** In $Cx30^{-/-}$ mice, DKG (100 μ M) restored synaptic glutamate to wild-type levels, as examined with γ -DGG **(b)**; DKG $n = 4$ cells, without DKG $n = 15$ cells (see **Fig. 1e**), $P = 0.0036$, $U = 3$, Mann-Whitney), increased mEPSC frequency **(c)**; $Cx30^{+/+}$ $n = 5$ cells, $P = 0.8061$, $t(4) = 0.2623$, $Cx30^{-/-}$ $n = 7$ cells, $P = 0.0055$, $t(6) = 4.235$, paired t -test), increased EPSC amplitude **(d)**; $Cx30^{+/+}$ $n = 22$ cells, $P = 0.1762$, $W = 85$, $Cx30^{-/-}$ $n = 17$ cells, $P = 0.0067$, $W = 111$, Wilcoxon matched pairs test) and rescued normal LTP magnitude when applied for 3 min before the tetanus **(e)**; $Cx30^{+/+}$ $n = 8$ slices, $Cx30^{-/-}$ $n = 7$ slices, $Cx30^{-/-}$ + DKG $n = 10$ slices; comparison 30–40 min after the tetanus, $P = 0.033$, $F(2) = 3.98645$, one-way ANOVA; *post hoc* Dunnett (comparison to $Cx30^{+/+}$ group), $Cx30^{-/-}$ $P = 0.0245$, $q = 2.695$, $Cx30^{-/-}$ + DKG $P = 0.744$, $q = 0.6466$). Same data for $Cx30^{-/-}$ and $Cx30^{+/+}$ mice as in **Figure 1g**. **(f)** Quantitative immunoblotting for GLT1 and GLAST showed similar total expression in $Cx30^{-/-}$ ($n = 3$ mice) and $Cx30^{+/+}$ ($n = 3$ mice) hippocampal extracts. **(g)** GLTs were similarly enriched in raft domains (identified by flotillin-1 accumulation) in $Cx30^{-/-}$ ($n = 6$ mice) and $Cx30^{+/+}$ ($n = 6$ mice) hippocampal extracts. Full-length blots are presented in **Supplementary Figure 8a,b**. **(h)** Protein distribution (%) in raft and non-raft fractions (GLT1: $P = 0.3418$, $t(10) = 0.9981$; GLAST: $P = 0.714$, $t(10) = 0.3770$; flotillin-1: $P = 0.2408$, $t(10) = 1.2471$, unpaired t test). **(i)** Functional surface expression of GLTs, assessed by whole-cell currents evoked by D-aspartate (1 s, 10 mM D-aspartate + 10 μ M CPP + 0.5 μ M TTX), was not altered in $Cx30^{-/-}$ astrocytes ($Cx30^{+/+}$ $n = 7$ cells, $Cx30^{-/-}$ $n = 8$ cells, $P = 0.815$, $t(13) = 0.2382$, unpaired t test). Scale bar, 50 pA and 10 s. All data are expressed as mean \pm s.e.m. * $P < 0.05$, ** $P < 0.01$.

for GLAST and GLT1, the two astroglial GLTs, revealed no change in total GLT levels from $Cx30^{-/-}$ whole hippocampi (protein levels normalized to tubulin; GLAST: $Cx30^{+/+}$, 2.7 ± 0.4 , $n = 3$ mice; $Cx30^{-/-}$, 2.9 ± 0.5 , $n = 3$ mice; $P = 0.2529$, $t(4) = 1.335$, unpaired t test; and GLT1: $Cx30^{+/+}$, 1.9 ± 0.05 , $n = 3$ mice; $Cx30^{-/-}$, 1.8 ± 0.2 , $n = 3$ mice; $P = 0.7960$, $t(4) = 0.2763$, unpaired t test; **Fig. 2f**) or isolated lipid raft compartments (**Fig. 2g,h**), where functional GLTs are enriched¹⁷ (**Supplementary Fig. 5a,b**). To further test for changes in the density of functional GLTs, we recorded whole-cell responses of astrocytes to a local saturating concentration of D-aspartate (10 mM, 1 s) in the presence of tetrodotoxin and 3-((R)-2-carboxypiperazin-4-yl)-propyl-1-phosphonic acid (CPP). The size of the evoked GLT currents in $Cx30^{-/-}$ mice was unchanged (**Fig. 2i**).

Although these data suggest a similar number of functional surface GLTs in $Cx30^{-/-}$ astrocytes, local alterations in GLT density specifically around synapses might remain undetected. Therefore, we further investigated whether increasing GLT density in astrocytes from

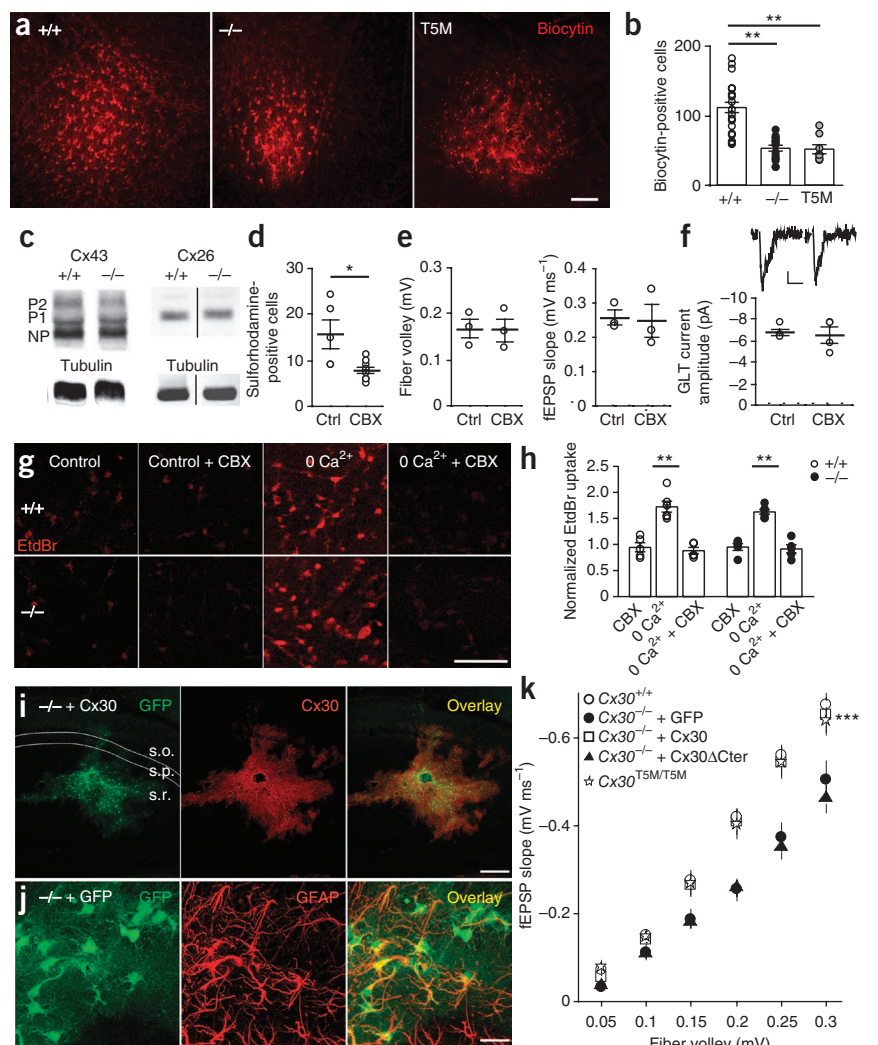
wild-type mice could mimic the decrease in excitatory synaptic transmission we found in $Cx30^{-/-}$ mice. For this, we took advantage of the β -lactam antibiotic ceftriaxone, which has been shown to enhance GLT1 expression and thereby alters neuronal plasticity and behavior, as well as offers neuroprotection^{18–20}, by modulating the activity of extrasynaptic glutamate receptors¹⁹. However, ceftriaxone treatment in wild-type mice had no effect on excitatory synaptic transmission of CA1 pyramidal neurons (**Supplementary Fig. 5c**). Thus, the alteration solely of total GLT levels is unlikely to account for the defects of synaptic transmission in $Cx30^{-/-}$ mice.

Cx30 non-channel function regulates synaptic transmission

Which function of Cx30, channel or non-channel, mediates the regulation of excitatory synaptic transmission? Because we found gap junctional communication decreased by $\sim 50\%$ in stratum radiatum astrocytes of $Cx30^{-/-}$ mice (**Fig. 3a,b**), and no compensatory regulation of Cx43 and Cx26 protein levels (**Fig. 3c**), we examined whether

Figure 3 Cx30-mediated effects are channel independent. (a,b) Reduction of gap junctional coupling in stratum radiatum astrocytes from $Cx30^{-/-}$ ($n = 16$ cells), $Cx30^{T5M/T5M}$ ($n = 8$ cells) compared to $Cx30^{+/+}$ ($n = 26$ cells) mice ($P < 0.0001$, $F(2) = 23.28677$, one-way ANOVA; *post hoc* Dunnett (comparison to $Cx30^{+/+}$ group), $Cx30^{-/-}$ $P < 0.001$, $q = 6.030$, $Cx30^{T5M/T5M}$ $P < 0.001$, $q = 4.855$), as revealed by biocytin diffusion. Scale bar, 100 μm . (c) Cx43 and Cx26 protein expression in $Cx30^{-/-}$ mice ($n = 3$ mice) was similar to that in wild-type mice ($n = 3$ mice). Phosphorylated isoforms 1 and 2 (P1, P2) and non-phosphorylated (NP) Cx43 are seen. Full-length blots are presented in **Supplementary Figure 8c**.

(d-f) Inhibition of gap junction communication in $Cx30^{+/+}$ astrocytes to $Cx30^{-/-}$ levels (by ~50%) by carbenoxolone (CBX, 10 μM , 10 min), as quantified by sulforhodamine B diffusion (d; $Cx30^{+/+}$ (Ctrl) $n = 5$ cells, $Cx30^{+/+}$ + CBX $n = 10$ cells, $P = 0.0113$, $U = 5$, Mann-Whitney) did not change neuronal transmission (e; $n = 3$ slices, fiber volley: $P = 0.8260$, $t(2) = 0.2499$, fEPSP slope: $P = 0.7642$, $t(2) = 0.3432$, paired t test) and astrocytic GLT currents (f; $n = 4$ cells, $P = 0.875$, $W = 2$, Wilcoxon matched pairs test). Scale bar, 1 pA and 20 ms. (g,h) Cx30 hemichannel-dependent uptake was not observed in astrocytes in control conditions: CBX (200 μM), a hemichannel blocker, had no effect on basal ethidium bromide uptake in $Cx30^{+/+}$ and $Cx30^{-/-}$ mice ($n = 5$ slices for both genotypes, $Cx30^{+/+}$ $P = 0.3810$, $U = 8$; $Cx30^{-/-}$ $P = 0.9444$, $U = 12$, Mann-Whitney), whereas removal of extracellular calcium (0 Ca^{2+}) did ($n = 6$ slices for both genotypes, $Cx30^{+/+}$ $P = 0.0022$, $U = 0$; $Cx30^{-/-}$ $P = 0.0022$, $U = 0$, Mann-Whitney), an effect inhibited by CBX ($n = 5$ slices for both genotypes, $Cx30^{+/+}$ $P = 0.500$, $U = 9$; $Cx30^{-/-}$ $P = 0.4444$, $U = 8.5$, Mann-Whitney). A control condition was included independently for each treatment and statistics were analyzed on raw data (comparison to control condition). Scale bar, 10 μm . (i) Local infection in stratum radiatum (s.r.) by astrocyte-targeted lentiviral vectors encoding GFP and full-length Cx30 (detected by immunohistochemistry, red; s.p., stratum pyramidale; s.o., stratum oriens). Scale bar, 150 μm . (j) Lentiviral vectors target astrocytes *in vivo*: they restricted transgene expression (GFP, green) almost exclusively to GFAP-positive cells (detected by immunohistochemistry, red). Scale bar, 25 μm . (k) Input-output curves for basal synaptic transmission in $Cx30^{+/+}$ mice ($n = 6$ slices), $Cx30^{T5M/T5M}$ mice ($n = 8$ slices) and $Cx30^{-/-}$ mice locally infected by lentiviral vectors encoding GFP only ($n = 11$ slices), or GFP and either full-length Cx30 ($n = 14$ slices) or Cx30 Δ Cter ($n = 13$ slices). Only expression of full-length Cx30 restored normal synaptic transmission in $Cx30^{-/-}$ mice (genotype: $P < 0.0001$, $F(4,294) = 36$; fiber volley: $P < 0.0001$, $F(5,294) = 328.9$, two-way ANOVA; *post hoc* uncorrected Fisher's LSD, fiber volley: 0.15 mV $P = 0.0176$, 0.2–0.3 mV $P < 0.001$, as compared to $Cx30^{-/-}$ + GFP). Excitatory transmission in $Cx30^{T5M/T5M}$ mice was comparable to that in $Cx30^{+/+}$ mice (*post hoc* uncorrected Fisher's LSD, fiber volley: 0.05 mV $P = 0.897$, 0.10 mV $P = 0.925$, 0.15 mV $P = 0.868$, 0.20 mV $P = 0.677$, 0.25 mV $P = 0.677$, 0.30 mV $P = 0.352$). All data are expressed as mean \pm s.e.m. * $P < 0.05$, ** $P < 0.01$, *** $P < 0.001$.



gap junction channels were involved in both synaptic transmission and glutamate clearance. To do so, we first reduced gap junction coupling in $Cx30^{+/+}$ mice to $Cx30^{-/-}$ levels (by ~50%) with carbenoxolone (CBX, 10 μM , **Fig. 3d**). However this did not reduce evoked fEPSPs (**Fig. 3e**) or increase synaptically evoked GLT currents in astrocytes (**Fig. 3f**). In addition, double-knockout mice for Cx30 and Cx43, totally devoid of gap junctional coupling, show no decrease in excitatory transmission²¹.

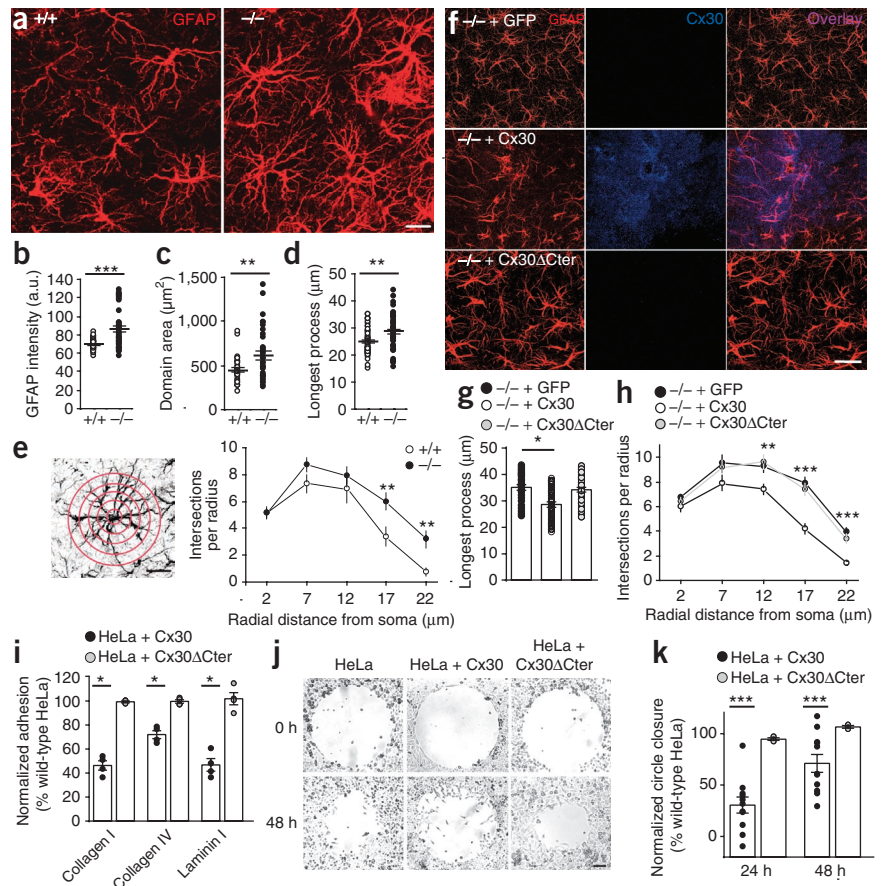
We furthermore excluded a contribution of Cx30 hemichannels because, under our physiological recording conditions, we did not detect functional Cx30 hemichannels in astrocytes, as assessed by ethidium bromide uptake (**Fig. 3g,h**). To further test the involvement of non-channel functions of Cx30, we investigated excitatory synaptic transmission in $Cx30^{T5M/T5M}$ mice, in which the replacement of a threonine by a methionine at position 5 of Cx30 leads to a

defective Cx30 channel pore but intact membrane targeting^{22,23}. We found in $Cx30^{T5M/T5M}$ mice that, despite the reduction of astroglial gap junctional communication by ~50%, as found in $Cx30^{-/-}$ mice (**Fig. 3a,b**), excitatory transmission of CA1 Schaffer collateral synapses was unchanged (**Fig. 3k**).

Because non-channel functions of connexin, such as intracellular signaling and cytosolic protein interactions, are mediated primarily by their intracellular C-terminal domain^{5,7}, we investigated whether this domain was involved in Cx30 regulation of synaptic transmission. We used a lentiviral vector targeting selectively astrocytes *in vivo*²⁴ to induce locally in the hippocampal CA1 area of $Cx30^{-/-}$ mice the expression of either full-length Cx30, C-terminally truncated Cx30 (Cx30 Δ Cter) or GFP (**Fig. 3i,j**). While lentivirally mediated restoration of Cx30 expression in stratum radiatum $Cx30^{-/-}$ astrocytes (**Fig. 3i**) rescued normal excitatory transmission, the Cx30 Δ Cter failed to do

Figure 4 Cx30 regulates cell morphology,

adhesion and migration. (a–e) GFAP immunoreactivity, in arbitrary units (a.u.), was increased in *Cx30*^{-/-} astrocytes (a,b; *Cx30*^{+/+} *n* = 59 cells, *Cx30*^{-/-} *n* = 42 cells, *P* < 0.0001, *t*(44.55) = 4.883, unpaired *t* test with Welch's correction) and revealed larger domain areas (c; *Cx30*^{+/+} *n* = 30 cells, *Cx30*^{-/-} *n* = 35 cells, *P* = 0.0054, *t*(52.88) = 2.901, unpaired *t* test with Welch's correction), elongated processes (d; *Cx30*^{+/+} *n* = 49 cells, *Cx30*^{-/-} *n* = 48 cells, *P* = 0.0025, *t*(86) = 3.116, unpaired *t* test with Welch's correction) and enhanced ramification (e; *Cx30*^{+/+} *n* = 12 cells, *Cx30*^{-/-} *n* = 17 cells; radial distance from soma 2 μm: *P* = 0.9747, *U* = 101; 7 μm: *P* = 0.1441, *U* = 69; 12 μm: *P* = 0.2640, *U* = 76.5; 17 μm: *P* = 0.0033, *U* = 38; 22 μm: *P* = 0.0011, *U* = 32.5; Mann-Whitney). Left (e), illustration of process measurements and Sholl analysis for intersection quantification in a GFAP-labeled astrocyte. Scale bar, 10 μm. (f) GFAP and Cx30 immunolabeling in hippocampal slices from *Cx30*^{-/-} mice (8 weeks old) infected with lentivirus encoding GFP, or GFP and either full-length Cx30 or Cx30ΔCter. Scale bar, 50 μm. (g,h) Wild-type morphology was rescued by full-length Cx30 (*n* = 40 cells), but not GFP (*n* = 30 cells) or Cx30ΔCter (*n* = 42 cells), as assessed by longest process length (g; *P* < 0.0001, *F*(2,109) = 13.77, one-way ANOVA; *post hoc* Dunnett (comparison to *Cx30*^{-/-} + GFP group), *Cx30*^{-/-} + Cx30 *P* < 0.0001, *q*(109) = 4.606; *Cx30*^{-/-} + Cx30ΔCter *P* = 0.759, *q*(109) = 0.6065) and process ramification (h; radial distance from soma 2 μm: *P* = 0.2889, KW = 2.483; 7 μm: *P* = 0.1800, KW = 3.429; 12 μm: *P* = 0.0096, KW = 9.302; 17 μm: *P* < 0.0001, KW = 29.37; 22 μm: *P* < 0.0001, KW = 24.79, Kruskal-Wallis; Dunn's *post hoc* test (comparison to *Cx30*^{-/-} + GFP group), *Cx30*^{-/-} + Cx30 12 μm: *P* = 0.0375, 17–22 μm: *P* < 0.0001, *Cx30*^{-/-} + Cx30ΔCter 12–17 μm: *P* = 1.00, 22 μm: *P* = 0.928). (i) Adhesion to different extracellular matrix components, measured as fluorescence of adherent cells, was reduced as compared to that of wild-type HeLa cells in HeLa cells expressing full-length Cx30 (*n* = 4 cultures; wild-type HeLa *n* = 4 cultures; *P* = 0.0286, *U* = 0 for all three conditions, Mann-Whitney), but not Cx30ΔCter (*n* = 4 cultures; wild-type HeLa *n* = 4 cultures; collagen I: *P* = 0.4857, *U* = 5; collagen IV: *P* > 0.9999, *U* = 8; laminin: *P* = 0.8286, *U* = 7; Mann-Whitney). A control condition was included independently for each treatment and statistical analysis was performed on raw data. (j) Cell migration illustrated by phase-contrast images of HeLa cell monolayers 0 h and 48 h after removal of a nonattachable gel spot. Scale bar, 100 μm. (k) Migration of HeLa cells expressing full-length Cx30 (*n* = 11 cultures) was delayed and inhibited as compared to that of wild-type HeLa cells (*n* = 11 cultures) (24 h: *P* ≤ 0.0001, *t*(20) = 6.000; 48 h: *P* = 0.0007, *t*(20) = 4.024; unpaired *t* test), as quantified by the closure of an open circle. In contrast, migration of Cx30ΔCter HeLa cells (*n* = 3 cultures) was similar to that of wild-type cells (*n* = 3 cultures) (24 h: *P* = 0.5536, *t*(4) = 0.6457; 48 h: *P* = 0.2670, *t*(4) = 1.289; unpaired *t* test). A control was performed independently for each condition and statistical analysis was performed on raw data. All data are expressed as mean ± s.e.m. **P* < 0.05, ***P* < 0.01, ****P* < 0.001.



so (Fig. 3k). Taken together, these results suggest that non-channel functions of Cx30, involving its C-terminal domain, mediate the regulation of synaptic transmission.

Cx30 controls cell morphology, adhesion and migration

Channel-independent functions of connexins include cell adhesion and protein interactions⁷, and Cx30 has recently been shown to interact with actin and tubulin²⁵. In addition, one determining factor of astroglial glutamate clearance is the glial coverage of neurons^{3,4,26}. We therefore investigated whether Cx30 regulates astroglial morphology. Astrocytic soma area and overall volume of proximal processes, detected by cytoplasmic S100 staining or sulforhodamine 101 labeling, were unchanged in *Cx30*^{-/-} astrocytes (Supplementary Fig. 6a–c). However, ultrastructural analysis using electron microscopy revealed that the total volume of astrocytic processes in the neuropil of the stratum radiatum region was increased by ~25% in *Cx30*^{-/-} mice (see below), suggesting an increased size and/or number of fine distal processes. In addition, GFAP immunoreactivity

was enhanced in hippocampal astrocytes from *Cx30*^{-/-} mice (Fig. 4a). This was not a result of reactive gliosis in *Cx30*^{-/-} mice, as confirmed by unchanged immunoreactivity for glutamine synthetase and for signal transducer and activator of transcription 3 (STAT3), as well as absence of vimentin staining and of intermediate filament accumulation as observed by electron microscopy (Supplementary Fig. 6d–h). Instead, increased GFAP levels revealed a larger domain area, elongated processes and enhanced ramification of *Cx30*^{-/-} astrocytes (Fig. 4a–e), as assessed by Sholl analysis.

How does Cx30 modulate astroglial morphology? As in the regulation of synaptic transmission, we found that the Cx30 C-terminal domain was necessary for the role of Cx30 in morphology, because the changes induced in *Cx30*^{-/-} astrocytes (increased GFAP, process elongation and ramification) were inhibited by lentivirally mediated expression of full-length Cx30, but not Cx30ΔCter (Fig. 4f–h). Because cell morphology strongly depends on adhesive properties²⁷ and other connexins have been shown to regulate adhesion independently of channel-mediated intercellular communication⁶,

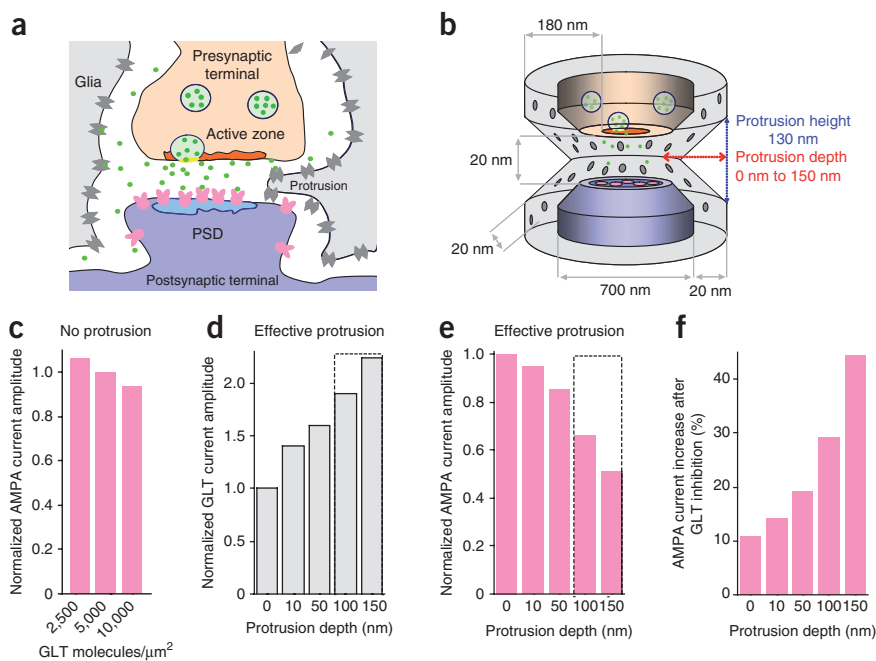


Figure 5 Astroglial process extension toward synaptic clefts enhances glutamate clearance and decreases AMPAR-mediated synaptic transmission. (a) Sketch of a synapse. After vesicle fusion, released glutamate (green) can be taken up by GLTs (gray), preventing glutamate from AMPAR binding (pink). (b) Synapse geometry used for simulation of AMPARs and GLTs after glutamate release. Astrocytic protrusions were raised from the glial sheath at varying depth such that protrusions of large depth penetrated the synaptic cleft. (c) Without protrusion, AMPAR currents were independent of GLT density. (d,e) Simulated GLT (gray) and AMPAR currents (pink), normalized to the situation with no astroglial protrusion. Protrusions with large depths (>100 nm) led to GLT current increase and AMPAR current decrease, and were thus defined as effective protrusions. (f) Increase of AMPAR current following GLT inhibition reveals regulative power of GLT-covered protrusions.

and because Cx30 regulated the extent of astroglial processes (Fig. 4a–h), we investigated whether an extension of these processes, highly enriched in GLTs¹⁶, toward synaptic clefts might enable them to access synaptic glutamate directly and thereby shape postsynaptic responses.

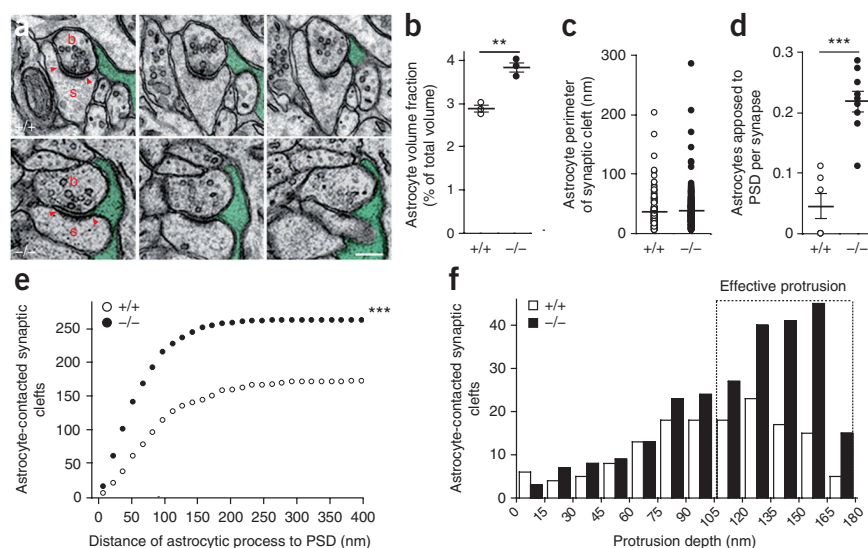
To do so, we first developed a mathematical model of a synapse surrounded by astroglial processes with membrane protrusions (Fig. 5a,b). We computed the glutamate flux to transporters and the number of open AMPARs as function of the astroglial protrusion depth and GLT density. Increasing GLT density from 2,500 to 10,000 per μm^2 on astrocytes without protrusion had hardly any influence on basal AMPAR currents (Fig. 5c), confirming previous studies¹⁹ and our current data showing that the ceftriaxone-induced increased astroglial GLT1 density in wild-type mice did not affect excitatory synaptic transmission of CA1 pyramidal neurons (Supplementary Fig. 5c).

we investigated whether Cx30 modifies cell adhesion to the extracellular matrix. We found adhesion to collagen and laminin strongly reduced in HeLa cells expressing Cx30, but not Cx30 Δ Cter (Fig. 4i). Furthermore cell migration was profoundly decreased in HeLa cells transfected with Cx30, but not Cx30 Δ Cter (Fig. 4j,k). Taken together, these data demonstrate that Cx30, through its C-terminal domain, controls cell morphology and motility.

Astroglial synapse invasion alters excitatory transmission

Because Cx30 regulation of synaptic strength through glutamate uptake does not involve the well-known modulation of extrasynaptic receptors controlling presynaptic release⁴ (Supplementary Fig. 3e)

Figure 6 Astrocytes deficient in Cx30 invade synaptic clefts. (a) Serial electron microscopy images showing astroglial processes (green) penetrating the synaptic cleft in the stratum radiatum of Cx30^{-/-} mice. PSD, arrowhead; axonal bouton, b; dendritic spine, s. Scale bar, 0.2 μm . (b) Astrocytes from Cx30^{-/-} mice ($n = 3$ tissue samples) occupied a larger volume of the neuropil than those from Cx30^{+/+} mice ($n = 3$ tissue samples, $P = 0.0024$, $t(4) = 6.798$, unpaired t test). (c) Astrocyte perimeter of the synaptic cleft was comparable ($P = 0.2864$, $U = 21671$, Mann-Whitney) in Cx30^{+/+} ($n = 176$ synapses) and Cx30^{-/-} mice ($n = 262$ synapses). (d) Number of astroglial protrusions apposed to PSDs per synapse in defined volume fractions was increased in Cx30^{-/-} mice ($P < 0.0001$, $t(13) = 6.323$, $n = 9$ tissue samples, unpaired t test) as compared to wild-type mice ($n = 6$ tissue samples). (e) In comparable stratum radiatum volume fractions from Cx30^{-/-} (428 μm^3) and Cx30^{+/+} mice (378 μm^3), cumulative distributions of astrocytic process distance to PSD in synaptic clefts contacted by astrocytes differed in Cx30^{-/-} mice ($n = 262$ synapses in 3 mice) from that in Cx30^{+/+} mice ($n = 176$ synapses in 3 mice) ($P < 0.0001$, KS = 0.90844, Kolmogorov-Smirnov). (f) Histogram of protrusion depth in synaptic clefts contacted by astrocytes. Effective astroglial protrusions (depth > 100 nm), competing with AMPA receptors for glutamate binding, were more abundant in stratum radiatum of Cx30^{-/-} mice ($n = 3$ mice) than in Cx30^{+/+} mice ($n = 3$ mice). Data are expressed as mean \pm s.e.m. in b,c,d. ** $P < 0.01$, *** $P < 0.001$.



However, by comparing the current responses for a synapse invaded by a protrusion of 150 nm depth to a synapse without astroglial protrusion, we found that AMPAR currents were diminished by ~50%, whereas GLT currents were more than doubled (Fig. 5d,e). We defined an 'effective' astroglial process protrusion as one able to increase GLT currents while decreasing AMPAR currents. To investigate the effect of transporters located on protrusions, we simulated AMPAR currents for blocked GLTs (Fig. 5f). Whereas blocking GLTs in the absence of protrusions increased AMPAR currents by only ~10%, this increase rose with the depth of invading protrusion and reached ~50% for a depth of 150 nm. Thus, only active transporters located on protrusions markedly influenced AMPAR currents.

Cx30 deficiency causes astroglial synaptic cleft invasion

To examine whether Cx30 deficiency reduces the distance of astroglial processes to the synapse, thus enabling them to compete with postsynaptic AMPARs for glutamate binding, as predicted by the model, we used electron microscopy (Fig. 6a). The increased total volume of astrocytic processes in the neuropil of the stratum radiatum region (Fig. 6b) suggests a change in the astrocytic coverage of synapses. However we did not find an increase in astrocyte perimeter of synaptic clefts (Fig. 6c), indicating no overall enhanced astroglial coverage of synaptic elements.

Nevertheless, further three-dimensional analysis from serial electron microscopy images revealed the insertion of Cx30 deficient astroglial processes into synaptic clefts (Fig. 6a and Supplementary Fig. 7). Indeed, we found an increase of ~5-fold in the number of astroglial processes in close proximity to PSDs; that is, visually identified as apposed to the edge of PSDs in Cx30^{-/-} mice (Fig. 6a,d and Supplementary Fig. 7), as well as an increased number of synaptic clefts contacted by astrocytes (Fig. 6e). In addition the distribution of the distances between PSD edge and astroglial processes revealed an extension of astroglial processes toward PSDs in Cx30^{-/-} mice (Fig. 6e,f and Supplementary Fig. 7). Finally, we also found that the number of effective astroglial protrusions, as defined by the model (i.e., > 100 nm depth), was strongly enhanced in Cx30^{-/-} mice (Fig. 6e,f).

DISCUSSION

By combining physiology, mathematical modeling and electron microscopy, we identified Cx30 in astrocytes as a key molecular determinant of astroglial coverage of synapses controlling synaptic efficacy and hippocampus-based contextual memory. By regulating the extent of astroglial processes contacting synaptic clefts, Cx30 controls the efficacy of glutamate clearance and thereby the synaptic strength of excitatory terminals, by directly setting synaptic glutamate levels. Unexpectedly, this unconventional role of Cx30 is channel independent and serves as a negative regulator for cell adhesion and migration. These findings extend the classical model of neuroglial interactions in which, up to now, astrocytes were generally considered extrasynaptic elements regulating synaptic transmission indirectly through activation of extrasynaptic receptors.

Cx30 controls neuroglial interactions at synapses

We found that Cx30 defined intimate neuroglial morphological interactions at the synapse by regulating the extent of astroglial processes into synaptic clefts. These processes may preferentially extend toward excitatory synapses, as CA1 pyramidal cells from Cx30^{-/-} mice displayed a selective impairment in glutamatergic transmission (Supplementary Fig. 1b) and glutamate is capable of inducing formation and extension of astroglial filopodia²⁸.

Unexpectedly, several lines of evidence indicated that this Cx30 function occurred independently of its channel function: (i) although Cx30 deletion in astrocytes reduced gap junction coupling by ~50%, inhibiting gap junction communication either acutely and partially in wild-type mice to Cx30^{-/-} levels (Fig. 3d-f) or chronically and totally in mice deficient for both Cx43 and Cx30 (ref. 21) did not mimic the changes in excitatory synaptic transmission and astroglial glutamate clearance from Cx30^{-/-} mice; in addition, chronic inhibition of astroglial gap junctions in culture does not lead to increased glutamate uptake²⁹; (ii) Cx30 hemichannels were not functional in our physiological conditions; and (iii) hippocampal excitatory transmission was normal in mice with defective Cx30 channels due to the Cx30T5M mutation. The Cx30 non-channel function we report here in the regulation of synaptic transmission was undetectable in our previous study of Cx30^{-/-}Cx43^{-/-} mice²¹ because the numerous additional alterations induced by complete loss of astroglial intercellular gap junctional communication resulting from Cx30 and Cx43 deletion, such as decreased potassium clearance and extracellular space volume or astroglial reactivity²¹, were massive and predominated.

Several channel-independent functions of connexins in glial cells have been reported involving cell adhesion or protein interactions^{6,7}. However, channel-independent functions of Cx30 have not been previously described. Recently, Cx30 was shown to interact with microtubules and cortical actin filaments²⁵, suggesting that the morphological alterations we found in Cx30^{-/-} astrocytes (process elongation and ramification) are due to modifications of the cytoskeleton, as observed with GFAP labeling (Fig. 4a). These modifications led *in vivo* to an increased volume of Cx30^{-/-} astrocytic processes, which extended to form fine filopodium-like protrusions contacting synaptic clefts. Thus Cx30, via its intracellular C-terminal domain, likely belongs to a molecular complex involved in cellular morphology and motility. Remarkably, consistent with the inhibitory function of Cx30 that we found in cell motility, a downregulation of Cx30 occurs during astrocyte transformation into highly motile glioma cells, which infiltrate the surrounding tissue by invadopodia, and reexpression of Cx30 in glioma cell lines results in reduced tumor growth³⁰.

Synaptic glutamate uptake relies on glial-synapse vicinity

Astroglial glutamate clearance is important for maintaining low extracellular glutamate levels and preventing spillover, which otherwise activates extrasynaptic receptors and neighboring synapses and thereby indirectly alters excitatory synaptic transmission¹⁶. Indeed several studies have shown in different models, by decreasing glutamate clearance either pharmacologically¹⁶ or through reduced physical coverage of neurons by astrocytes⁴, that astrocytic GLTs indirectly regulate excitatory synaptic transmission by limiting the activation of extrasynaptic mGluRs, thereby increasing release probability. However, increasing functional glutamate uptake in astrocytes has been challenging as a result of the lack of selective tools. Only recently have a few studies investigated the impact of enhanced GLT expression on neurotransmission, either by using ceftriaxone, a β -lactam antibiotic^{19,20}, or by interfering with neuroglial EphA4-ephrin-A3 signaling^{31,32}. Both manipulations lead to an impairment of information processing, including alterations in prepulse inhibition of the startle reflex¹⁸, CA3 (ref. 19) and CA1 (ref. 32) long-term plasticity, and learning and memory performance³¹. Altered synaptic plasticity is due to reduced glutamate levels, preventing activation of presynaptic autoreceptors (mGluRs and kainate), which control transmitter release. However, the selective role of increased glutamate clearance remains unclear, as neuroglial EphA4-ephrin-A3 signaling also alters

dendritic spine morphology³³. Remarkably, basal excitatory synaptic transmission is normal in these models^{19,32}, confirming our modeling and experimental results demonstrating that increasing GLT density on wild-type astrocytes lacking protrusions contacting synaptic clefts has no effect on AMPAR currents (Fig. 5c and Supplementary Fig. 5c, respectively).

Therefore, up to now, a direct major impact of astrocytic glutamate clearance on the postsynaptic response, through changes in synaptic glutamate levels, has not to our knowledge been reported. Indeed, acute pharmacological inhibition of GLTs in wild-type mice does not affect, or only slightly changes, AMPA and NMDA current amplitudes and kinetics¹⁶. However, several properties confer on GLTs the ability to influence synaptic transmission by capturing synaptically released glutamate before it reaches the postsynaptic element: (i) they have high affinity for glutamate, comparable to that of NMDARs; (ii) they bind glutamate as fast as AMPARs (less than 1 ms); (iii) their density at astroglial membranes exceeds by far the density of postsynaptic AMPARs; (iv) the majority of hippocampal synapses (~60%) are contacted by astrocytic processes containing GLTs³⁴; and finally, (v) even though the cycling time of GLTs (~70 ms) is too slow to interfere with fast synaptic transmission, their buffering of glutamate molecules can circumvent postsynaptic receptors activation¹⁶. Despite such properties, GLTs fail to efficiently take up synaptic glutamate because they are generally too far from synaptic clefts. By changing the distribution of astroglial processes contacting PSDs, we uncovered a mechanism by which GLTs sufficiently close to the active zone of the synapse can directly depress the AMPAR-mediated postsynaptic response by lowering synaptic glutamate levels, and hence set the magnitude of excitatory transmission. Our data indicate that such proximity is regulated by astroglial Cx30. Indeed, although Cx30 is also at play in other cell types outside the brain, where it has been proposed to contribute to regulation of heart rate³⁵ and hearing^{36,37}, several lines of evidence indicate that the alteration of synaptic transmission is specific to Cx30 deficiency in astrocytes, as (i) synaptic transmission in *Cx30*^{-/-} mice was normal before Cx30 expression onset in astrocytes, (ii) restoring at later stages Cx30 expression selectively in astrocytes from *Cx30*^{-/-} mice was sufficient to rescue both normal astroglial morphology and synaptic transmission, (iii) reducing acutely astroglial glutamate uptake in *Cx30*^{-/-} mice to match wild-type levels restored normal synaptic glutamate, excitatory transmission and LTP, and (iv) during LTP induction, bypassing the insufficient synaptic glutamate levels using a pairing protocol coupling direct depolarization of the postsynaptic cell to synaptic stimulation restored normal LTP in *Cx30*^{-/-} mice.

Notably, the observed alterations in AMPA miniature and evoked currents, as well as in LTP, with no change in synapse number and pyramidal cell excitability, identify astrocytic GLTs as regulators of the moment-to-moment spontaneous and evoked basal synaptic transmission and plasticity in *Cx30*^{-/-} mice. Astroglial GLTs in *Cx30*^{-/-} mice were not saturated by synaptically released glutamate, even during high-frequency stimulation (100 Hz) performed to induce LTP, as reported in wild-type mice¹⁶, because we found that inhibition of astroglial GLTs to wild-type levels by DHK during LTP induction restored normal LTP in *Cx30*^{-/-} mice. The defect in LTP in *Cx30*^{-/-} mice therefore arose from an induction impairment due to the enhanced astroglial GLT activity. This resulted in insufficient synaptic glutamate levels to induce proper postsynaptic activation, as direct depolarization of the postsynaptic cell paired to 2-Hz synaptic stimulation fully restored normal LTP in *Cx30*^{-/-} mice. Interestingly, previous work had already proposed enhanced glutamate uptake—by neurons, however—as a limiting factor in LTP³⁸. Finally, insofar as

long-term memory of association between unconditioned stimuli and context engages the hippocampal circuitry¹⁵, the marked deficit of *Cx30*^{-/-} mice in contextual fear conditioning suggests that the regulation of astroglial GLT proximity to the active zone is a crucial mechanism ensuring optimal activation of the hippocampus upon cognitive demand.

Dynamics and plasticity of astrocytic processes

Our data, showing that Cx30 ensures efficient synaptic strength, suggest that Cx30, whose expression starts during late brain development (>P10)⁸, contributes to the maturation of efficient synaptic communication by hindering astrocytic processes from entering synaptic clefts and accessing glutamate. Indeed, in *Cx30*^{-/-} mice, the occurrence of fine astrocytic processes invading synaptic clefts was massively increased, and was associated with a decrease in AMPAR-mediated synaptic transmission.

Our mathematical model of the tripartite synapse predicts that GLT-containing astrocytic processes penetrating the synaptic cleft to a depth of at least 100 nm can produce the depression of excitatory transmission we measured. This computed process depth is compatible with recent data showing that, in wild-type mice, GLT-containing astrocytic processes are found in a range of 0–400 nm from the active zone^{19,39}. Furthermore, the model confirmed that inhibiting GLTs¹⁶ or increasing their density^{19,32} on wild-type extrasynaptic astrocytes (referred to as without protrusion) has no or only little effect on basal excitatory transmission, as predicted by other computational models^{40,41} and revealed by our experimental data (Fig. 2c,d and Supplementary Fig. 5c). Although we cannot exclude the possibility that fine astrocytic processes contacting PSDs may selectively express more GLTs in *Cx30*^{-/-} mice, it is only because the astroglial processes are closer to synapses that such putatively enhanced GLT density would additionally contribute to the decreased excitatory transmission. Astroglial protrusions invading synaptic clefts may well be a new dynamic mechanism altering basic cognitive functions, as our data indicated that Cx30 deficiency led to a loss of contextual memory. Astrocytic processes are plastic elements that are more motile than dendritic spines⁴², rapidly extending and retracting from synapses through actin cytoskeleton reorganization. Remarkably, enriched environment¹⁴ and kainate-induced seizures⁴³ increase Cx30 expression. Conversely, Cx30 is decreased in reactive astrocytes during excitotoxic injury⁴⁴, in astrocyte transformation into highly motile glioma cells³⁰ and in brains of patients with major depression⁴⁵ and of suicide completers⁴⁶. In all, this suggests an activity-dependent regulation of Cx30, controlling the dynamics of fine astrocytic processes binding glutamate to alter cognitive functions and behavior.

METHODS

Methods and any associated references are available in the [online version of the paper](#).

Note: Any Supplementary Information and Source Data files are available in the online version of the paper.

ACKNOWLEDGMENTS

We thank R. Nicoll, A. Koulakoff, E. Brouillet, O. Chever, F. Mammano and D. Schmitz for discussions and for technical assistance. This work was supported by grants from the Human Frontier Science Program Organization (Career Development Award), French Research Agency (Programme Jeunes chercheurs and Programme Blanc), City of Paris (Programme Emergence) and INSERM to N.R., from CEA and CNRS to C.E. and N.D., from International Brain Research Organization to V.A., from the French Research Ministry and Deutsche Forschungsgemeinschaft to U.P., from Labex Memolife to G.D., from the doctoral school ED3C, Paris 6 University to G.G. and from the Max-Planck Society to D.F.

AUTHOR CONTRIBUTIONS

G.G., C.E., P.E., M.C.-S. and K.B. contributed equally to this work. Conception and experimental design: N.R., U.P., D.H., G.D., D.F., G.K., C.E., K.B., M.C.-S.; Methodology and data acquisition: U.P., N.R., D.F., G.D., D.H., G.K., C.E., N.D., K.B., M.C.-S., G.G., V.A., P.E.; Analysis and interpretation of data: U.P., N.R., D.F., G.D., D.H., G.K., C.E., K.B., M.C.-S., G.G., V.A., P.E., A.D., J.H.R.L.; Manuscript writing and revision: N.R., U.P., G.D., D.H., G.K., C.E., K.B., J.H.R.L.

COMPETING FINANCIAL INTERESTS

The authors declare no competing financial interests.

Reprints and permissions information is available online at <http://www.nature.com/reprints/index.html>.

- Perea, G., Navarrete, M. & Araque, A. Tripartite synapses: astrocytes process and control synaptic information. *Trends Neurosci.* **32**, 421–431 (2009).
- Genoud, C. *et al.* Plasticity of astrocytic coverage and glutamate transporter expression in adult mouse cortex. *PLoS Biol.* **4**, e343 (2006).
- Iino, M. *et al.* Glia-synapse interaction through Ca²⁺-permeable AMPA receptors in Bergmann glia. *Science* **292**, 926–929 (2001).
- Oliet, S.H., Piet, R. & Poulain, D.A. Control of glutamate clearance and synaptic efficacy by glial coverage of neurons. *Science* **292**, 923–926 (2001).
- Pannasch, U. & Rouach, N. Emerging role for astroglial networks in information processing: from synapse to behavior. *Trends Neurosci.* **36**, 405–417 (2013).
- Elias, L.A., Wang, D.D. & Kriegstein, A.R. Gap junction adhesion is necessary for radial migration in the neocortex. *Nature* **448**, 901–907 (2007).
- Theis, M., Sohl, G., Eiberger, J. & Willecke, K. Emerging complexities in identity and function of glial connexins. *Trends Neurosci.* **28**, 188–195 (2005).
- Nagy, J.I., Patel, D., Ochalski, P.A. & Stelmack, G.L. Connexin30 in rodent, cat and human brain: selective expression in gray matter astrocytes, co-localization with connexin43 at gap junctions and late developmental appearance. *Neuroscience* **88**, 447–468 (1999).
- Harris, A.L. Emerging issues of connexin channels: biophysics fills the gap. *Q. Rev. Biophys.* **34**, 325–472 (2001).
- Roux, L., Benchenane, K., Rothstein, J.D., Bonvento, G. & Giaume, C. Plasticity of astroglial networks in olfactory glomeruli. *Proc. Natl. Acad. Sci. USA* **108**, 18442–18446 (2011).
- Dere, E. *et al.* Connexin30-deficient mice show increased emotionality and decreased rearing activity in the open-field along with neurochemical changes. *Eur. J. Neurosci.* **18**, 629–638 (2003).
- Frisch, C. *et al.* Mice with astrocyte-directed inactivation of connexin43 exhibit increased exploratory behaviour, impaired motor capacities, and changes in brain acetylcholine levels. *Eur. J. Neurosci.* **18**, 2313–2318 (2003).
- Theis, M. *et al.* Accelerated hippocampal spreading depression and enhanced locomotor activity in mice with astrocyte-directed inactivation of connexin43. *J. Neurosci.* **23**, 766–776 (2003).
- Rampon, C. *et al.* Effects of environmental enrichment on gene expression in the brain. *Proc. Natl. Acad. Sci. USA* **97**, 12880–12884 (2000).
- Ji, J. & Maren, S. Hippocampal involvement in contextual modulation of fear extinction. *Hippocampus* **17**, 749–758 (2007).
- Tzingounis, A.V. & Wadiche, J.I. Glutamate transporters: confining runaway excitation by shaping synaptic transmission. *Nat. Rev. Neurosci.* **8**, 935–947 (2007).
- Buttcher, M.E., Tian, G., Guo, H. & Lin, C.L. Association of excitatory amino acid transporters, especially EAAT2, with cholesterol-rich lipid raft microdomains: importance for excitatory amino acid transporter localization and function. *J. Biol. Chem.* **279**, 34388–34396 (2004).
- Bellei, M., Melone, M., Gubbini, A., Battistacci, S. & Conti, F. GLT-1 upregulation impairs prepulse inhibition of the startle reflex in adult rats. *Glia* **57**, 703–713 (2009).
- Omrani, A. *et al.* Up-regulation of GLT-1 severely impairs LTD at mossy fibre-CA3 synapses. *J. Physiol. (Lond.)* **587**, 4575–4588 (2009).
- Rothstein, J.D. *et al.* Beta-lactam antibiotics offer neuroprotection by increasing glutamate transporter expression. *Nature* **433**, 73–77 (2005).
- Pannasch, U. *et al.* Astroglial networks scale synaptic activity and plasticity. *Proc. Natl. Acad. Sci. USA* **108**, 8467–8472 (2011).
- Grifa, A. *et al.* Mutations in GJB6 cause nonsyndromic autosomal dominant deafness at DFNA3 locus. *Nat. Genet.* **23**, 16–18 (1999).
- Schütz, M. *et al.* The human deafness-associated connexin 30 T5M mutation causes mild hearing loss and reduces biochemical coupling among cochlear non-sensory cells in knock-in mice. *Hum. Mol. Genet.* **19**, 4759–4773 (2010).
- Colin, A. *et al.* Engineered lentiviral vector targeting astrocytes *in vivo*. *Glia* **57**, 667–679 (2009).
- Qu, C., Gardner, P. & Schrijver, I. The role of the cytoskeleton in the formation of gap junctions by Connexin 30. *Exp. Cell Res.* **315**, 1683–1692 (2009).
- Saab, A.S. *et al.* Bergmann glial AMPA receptors are required for fine motor coordination. *Science* **337**, 749–753 (2012).
- Parsons, J.T., Horwitz, A.R. & Schwartz, M.A. Cell adhesion: integrating cytoskeletal dynamics and cellular tension. *Nat. Rev. Mol. Cell Biol.* **11**, 633–643 (2010).
- Cornell-Bell, A.H., Thomas, P.G. & Smith, S.J. The excitatory neurotransmitter glutamate causes filopodia formation in cultured hippocampal astrocytes. *Glia* **3**, 322–334 (1990).
- Ozog, M.A., Siushansian, R. & Naus, C.C. Blocked gap junctional coupling increases glutamate-induced neurotoxicity in neuron-astrocyte co-cultures. *J. Neuropathol. Exp. Neurol.* **61**, 132–141 (2002).
- Princen, F. *et al.* Rat gap junction connexin-30 inhibits proliferation of glioma cell lines. *Carcinogenesis* **22**, 507–513 (2001).
- Carmona, M.A., Murai, K.K., Wang, L., Roberts, A.J. & Pasquale, E.B. Glial ephrin-A3 regulates hippocampal dendritic spine morphology and glutamate transport. *Proc. Natl. Acad. Sci. USA* **106**, 12524–12529 (2009).
- Filosa, A. *et al.* Neuron-glia communication via EphA4/ephrin-A3 modulates LTP through glial glutamate transport. *Nat. Neurosci.* **12**, 1285–1292 (2009).
- Murai, K.K., Nguyen, L.N., Irie, F., Yamaguchi, Y. & Pasquale, E.B. Control of hippocampal dendritic spine morphology through ephrin-A3/EphA4 signaling. *Nat. Neurosci.* **6**, 153–160 (2003).
- Witcher, M.R., Kirov, S.A. & Harris, K.M. Plasticity of perisynaptic astroglia during synaptogenesis in the mature rat hippocampus. *Glia* **55**, 13–23 (2007).
- Gros, D. *et al.* Connexin 30 is expressed in the mouse sino-atrial node and modulates heart rate. *Cardiovasc. Res.* **85**, 45–55 (2010).
- Cohen-Salmon, M. *et al.* Connexin30 deficiency causes intrastrial fluid-blood barrier disruption within the cochlear stria vascularis. *Proc. Natl. Acad. Sci. USA* **104**, 6229–6234 (2007).
- Teubner, B. *et al.* Connexin30 (Gjb6)-deficiency causes severe hearing impairment and lack of endocochlear potential. *Hum. Mol. Genet.* **12**, 13–21 (2003).
- Scimemi, A., Tian, H. & Diamond, J.S. Neuronal transporters regulate glutamate clearance, NMDA receptor activation, and synaptic plasticity in the hippocampus. *J. Neurosci.* **29**, 14581–14595 (2009).
- Melone, M., Bellei, M. & Conti, F. Synaptic localization of GLT-1a in the rat somatic sensory cortex. *Glia* **57**, 108–117 (2009).
- Barbour, B. An evaluation of synapse independence. *J. Neurosci.* **21**, 7969–7984 (2001).
- Zheng, K., Scimemi, A. & Rusakov, D.A. Receptor actions of synaptically released glutamate: the role of transporters on the scale from nanometers to microns. *Biophys. J.* **95**, 4584–4596 (2008).
- Haber, M., Zhou, L. & Murai, K.K. Cooperative astrocyte and dendritic spine dynamics at hippocampal excitatory synapses. *J. Neurosci.* **26**, 8881–8891 (2006).
- Condorelli, D.F. *et al.* Connexin-30 mRNA is up-regulated in astrocytes and expressed in apoptotic neuronal cells of rat brain following kainate-induced seizures. *Mol. Cell. Neurosci.* **21**, 94–113 (2002).
- Koulakoff, A., Ezan, P. & Giaume, C. Neurons control the expression of connexin 30 and connexin 43 in mouse cortical astrocytes. *Glia* **56**, 1299–1311 (2008).
- Bernard, R. *et al.* Altered expression of glutamate signaling, growth factor, and glia genes in the locus coeruleus of patients with major depression. *Mol. Psychiatry* **16**, 634–646 (2011).
- Ernst, C. *et al.* Dysfunction of astrocyte connexins 30 and 43 in dorsal lateral prefrontal cortex of suicide completers. *Biol. Psychiatry* **70**, 312–319 (2011).

ONLINE METHODS

Animals. Experiments were carried out according to the guidelines of the European Community Council Directives of January 1st 2013 (2010/63/EU) and of the local animal welfare committee (certificate A751901, Ministère de l'Agriculture et de la Pêche), and all efforts were made to minimize the number of animals used and their suffering. Animals were group housed on a 12 h light/dark cycle. *Cx30*^{-/-} mice were generated as previously described³⁷ and provided by K. Willecke, University of Bonn, Germany. Heterozygous mice carrying the knockout mutation were interbred to obtain the homozygous strain. *Cx30*^{T5M/T5M} mice²³ were provided by F. Mammano, Venetian Institute of Molecular Medicine, Italy. All mice were backcrossed to the C57BL6 background. Mice of both sexes and littermates were used at postnatal days 16–25, unless otherwise stated. The data presented in this manuscript were collected on 317 mice.

Antibodies, immunohistochemistry and immunoblotting. All the antibodies used in this study are commercially available and have been validated in previous studies, as reported by the suppliers. The following primary antibodies were used: GLT1 (1:2,000; AB1783) and GLAST (1:2,000; AB1782) guinea pig polyclonal antibodies, NeuN (1:500; MAB377) mouse monoclonal antibody, vimentin (1:20; AB1620) goat polyclonal antibody (Chemicon); GLT1 (1:10,000; Af670-1) and GLAST (1:10,000; Af660) rabbit polyclonal antibodies (Frontier Science Co); GLT1 (1:10,000; SC15317) goat polyclonal antibody (Santa Cruz); PSD95 (1:200; 610495) and flotillin-1 (1:500; 610820) mouse monoclonal antibody (BD Transduction Labs); synaptophysin (1:500; A0010) rabbit polyclonal antibody (Dakocytomation); S100 (1:2,000; 2644) rabbit polyclonal antibody, GFAP (1:2,000; G3893) rabbit polyclonal antibody, tubulin (1:10,000; T6199) mouse monoclonal antibody, anti-V5 (1:500; V8012) monoclonal antibody and β -actin (1:10,000; A5316) mouse monoclonal antibody (Sigma); Cx43 (1:500; 71-0700) and Cx30 (1:500; 71-2200) rabbit polyclonal antibodies (Zymed Laboratories); and Cx26 (1:500; 71-0500) rabbit polyclonal antibody (Invitrogen). The following HRP-conjugated secondary antibodies were used: donkey anti rabbit IgG (1:2,500; NA934; Amersham Biosciences), goat anti-guinea pig IgG (1:2,500; GTX26908; Gene Tex), goat anti-mouse IgG (1:2,500; SC2005; Santa-Cruz). The following fluorescent dye-conjugated secondary antibodies were used in appropriate combinations: goat anti-mouse IgG conjugated to Alexa 488 or 555 (1:2,000; A11029 or A21424), goat anti-rabbit IgG conjugated to Alexa 488 or 555 (1:2,000; A11024 or A21429) (Molecular Probes) or donkey anti-guinea pig conjugated to rhodamine (1:2,000; AP 193R; Chemicon). Immunohistochemistry and quantification were performed as previously described²¹. We here briefly summarize how the experiment was performed and quantified. Mouse hippocampal tissues were isolated, and rafts were purified by 1 h incubation in 1% Brij-58 at 4 °C and fractionation through a discontinuous sucrose gradient¹⁷. From the top of the gradient, ten fractions (400 μ l) and the pellet were collected, and protein abundance was quantified in each fraction. An equal volume of each fraction was diluted in a loading buffer and used for immunoblotting. Fractions corresponding to raft microdomains (fractions 3–5) and fractions corresponding to detergent-soluble material (fractions 8–10) were pooled and were then loaded on the same 10% PAGE gel to quantify the GLT distribution in the two pools (as a percentage of total proteins (100% = raft + non-raft fractions)), as illustrated in **Figure 2h**. Protein content was quantified in each fraction (raft and non-raft). Films were then scanned, and optical densities were measured after background subtraction using ImageJ software. Specific optical densities were normalized to the protein content of the corresponding fraction (in micrograms). A partition ratio, as illustrated in **Figure 2h**, was calculated as the ratio of normalized abundance of the GLT protein (GLAST or GLT1) in raft fractions to the normalized abundance in raft and soluble fractions (that is, total abundance) and was expressed as a percentage, as previously described⁴⁷. The illustrated non-raft partition in percent is then calculated by subtracting the raft partition from 100%. For quantification of the blots, we had to set the exposure time to get non-saturated bands for all fractions and samples. In these conditions, nearly undetectable bands were found for GLAST in non-raft fractions, in accordance with a previous report¹⁷. Such nearly undetectable bands for non-raft GLAST were observed in both wild-type and Cx30 KO mice.

For analysis of astrocytic ramification, we used an adaptation of Sholl's concentric circles technique. Briefly, five circles at 5- μ m intervals were drawn around each astrocyte; the circle enclosing the soma had a diameter of 8 μ m and the soma was assumed to be 6 μ m. The number of intersections of astrocytic processes with

each circle was quantified. The longest primary process was measured by tracing the process with the ImageJ length measuring tool. Cell soma size was measured in ImageJ on overlaid projections of several consecutive images by delineating the visible cell body area. Sulforhodamine 101 (SR101) labeling of astrocytes, immunoblotting of hippocampi²¹ and isolation and quantification of lipid rafts⁴⁷ were performed as previously described.

Dye uptake by hemichannels. The hemichannel-permeable fluorescent tracer ethidium bromide (EtdBr, 314 Da) was included in either ACSF or ACSF with no Ca²⁺ and 5 mM EGTA at a final concentration of 4 μ M. Slices were incubated for 10 min in the solutions (equilibrated with 95% O₂ and 5% CO₂ at room temperature). In blocking experiments, slices were preincubated 15 min before and during EtdBr application with the gap junction and connexin/pannexin hemichannel blocker carbenoxolone (CBX, 200 μ M). Slices were then rinsed 15 min in ACSF, fixed for 2 h in 4% paraformaldehyde in 0.12 M phosphate buffer and mounted in Fluoromount. Labeled cells were visualized with a 40 \times objective in a Leica microscope (DMRB) equipped with epifluorescence illumination and appropriate filters for EtdBr (excitation wavelength, 528 nm; emission wavelength, 598 nm). Fluorescence images were captured with a Nikon Digital Camera (DXM 1200) and an imaging system (NIS-Elements AR 2.30 software). Labeled cells were also examined in a confocal laser-scanning microscope (TCS SP5, Leica, Germany) with a 63 \times objective. Stacks of consecutive confocal images were taken at 300 nm intervals and acquired with a laser (561 nm); z projections were reconstructed using the LAS AF software. At least three fields were selected in each slice. Fluorescence was digitized in arbitrary units (a.u.) with image-processing software. Dye uptake was expressed as the difference between the fluorescence measured in cells (20–30 per slice) and the background fluorescence measured where no labeled cells were detected. Values of fluorescence in different experimental conditions were normalized to the control level.

Lentivirus production and injection. We produced self-inactivated (SIN) lentiviruses containing the central polypurine tract (cPPT) sequence, the mouse phosphoglycerate kinase I promoter (PGK), the woodchuck post-regulatory element (WPRE) sequence and the target sequence of miR124 as previously described²⁴. We used the Gateway system (Invitrogen) to clone cDNA of GFP, mouse *Cx30* and mouse *Cx30* Δ Cter from the pENTR-D-TOPO plasmid (Invitrogen) into the SIN-cPPT-PGK-Gateway-WPRE-miR124T plasmid. Viruses (lenti-GFP, lenti-Cx30 and lenti-Cx30 Δ Cter) were produced in 293T cells using a four-plasmid system as previously described⁴⁷ and were pseudotyped with the G protein of the mokola lyssavirus²⁴. *Cx30*^{-/-} mice (age 3–4 weeks) were anesthetized with a mixture of ketamine (15 mg/kg) and xylazine (1.5 mg/kg) and placed on a stereotaxic frame under body temperature monitoring. Lentiviral vectors were diluted in PBS with 1% BSA at a concentration of 100 ng p24 per μ l and were injected bilaterally into the hippocampus at a rate of 0.2 μ l/min, using a 34-gauge blunt-tip needle linked to a Hamilton syringe by a polyethylene catheter. Lenti-Cx30 or lenti-Cx30 Δ Cter (160 ng p24 per site) were mixed with lenti-GFP (200 ng p24 per site) to detect the infection area. The stereotaxic coordinates were, from bregma, anteroposterior, -2 mm; lateral, \pm 2 mm; and ventral, -1.5 mm from the dura, with the tooth bar set at 0 mm.

At the end of the injection, the needle was left in place for 5 min before being slowly removed. The skin was sutured and mice were allowed to recover for 4 weeks before experiments were performed. With the dose of lentiviral vector and injection conditions used in this study, no astrogliosis was observed. Astroglial morphology was analyzed at a distance of ~150–200 μ m from the injection site and the images were taken at the same distance. Quantification of immunofluorescence stainings confirmed that these mokola-miR124T lentiviral vectors led to a selective infection of astrocytes, as the infected cells were positive for the GFAP astrocytic marker (lenti-Cx30: 98 \pm 2%, *n* = 3; lenti-GFP: 97 \pm 3%, *n* = 3) but not for markers of neurons (NeuN, lenti-Cx30 and lenti-GFP: 0%, *n* = 3), oligodendrocyte precursors (NG2, lenti-Cx30 and lenti-GFP: 0%, *n* = 3) or microglial cells (IBA1, lenti-Cx30 and lenti-GFP: 0%, *n* = 3) (*n* refers to the number of tested animals).

Astrocyte and HeLa cell cultures. Astrocytes and HeLa cells, an immortal human cell line derived from cervical cancer, were grown on Dulbecco's modified Eagle's medium (Invitrogen) supplemented with 10% FCS, in 5% CO₂ at 37 °C. Stable transfections were carried out for HeLa cells, while infections

by the lentiviral vectors described above or transient transfections were performed for astrocytes. The *Cx30ΔCter* insert was amplified by PCR on mouse 129Sv genomic DNA, as it is contained in a single exon, using the following primers: Forward, 5'-ACGATGGACTGGGGGACCCTGC-3'; Reverse, 5'-CTGCTTCTCTCTTCAGGGCATG-3'. They were cloned into pcDNA3.1V5-His (Invitrogen). The sequence was verified on both strands. *Cx30ΔCter*, like *Cx30*, led to protein expression, was targeted to cell membranes and formed gap junction plaques, which resulted in functional gap junctional coupling.

Adhesion and migration assays. Adhesion of HeLa cells was tested on different extracellular matrix components using the CytoSelect 48-Well Cell Adhesion Assay from Cell Biolabs. The assay was performed according to the manufacturer's protocol. 100,000 cells per well were seeded. Migration of HeLa cells was tested with the Radius cell migration assay from Cell Biolabs, performed according to the manufacturer's protocol. Migration was monitored with an inverted microscope at different time points. Cells were kept in 0.5% serum throughout the experiment to reduce proliferation. Analysis of the open area was performed with Tscratch.

Serial section electron microscopy. To prepare hippocampal tissue for ultrastructural analysis using serial section electron microscopy, we used the same protocol that has been described previously². Serial electron microscopic images were taken using a digital camera (Morada, Olympus) mounted in a Philips CM10 transmission electron microscope using an acceleration voltage of 80 kV. Images were aligned using Photoshop software (Adobe, San Jose, California, United States), and analyzed with ImageJ software (NIH, USA). Astrocytic profiles are clearly identifiable in serial digital images owing to their pale cytoplasm, irregular contouring borders and the absence of vesicles as well as synapses. Only asymmetric synapses identified by the shape of their pre- and postsynaptic densities and their synaptic vesicles (Gray type 1 versus Gray type 2 synapses) were included in the quantification. The total astrocytic volume was measured by delineating their processes in every image. This was carried out in volumes from *Cx30^{+/+}* mice ($n = 3$, 378 μm^3) and *Cx30^{-/-}* mice ($n = 3$, 428 μm^3). These volumes did not include any large dendritic profiles or somata of neurons, glia or endothelial cells. To quantify astrocyte–synaptic cleft contacts, only astrocytic process endings visually directly apposed to postsynaptic densities (PSD)—i.e. with no intervening elements of the neuropil—were counted in randomly selected fields of 4 μm^2 and 1.3 μm thickness (volume 5.2 μm^3) in six *Cx30^{+/+}* and nine *Cx30^{-/-}* stratum radiatum blocks. The number of dendritic spines was also analyzed in these volumes.

A more detailed analysis of electron micrographs was performed in Fiji, a free program based on ImageJ. Surface areas of cross-sectioned PSDs were computed by measuring their lengths on individual sections, multiplying by section thickness, and summing over all sections where the PSD was visible. Astrocyte-PSD distance measurements were carried out in similar total volumes of *Cx30^{+/+}* mice ($n = 3$, 378 μm^3) and *Cx30^{-/-}* mice ($n = 3$, 428 μm^3) and were only performed on synapses where fine astrocytic processes were clearly visible at the synaptic cleft (*Cx30^{+/+}* $n = 176$ synapses; *Cx30^{-/-}* $n = 262$ synapses) and in the section where the astrocytic membrane was closest to the PSD. Cross-sectioned astroglial perimeters of the synaptic cleft were computed by assigning the contact point between the astrocytic membrane and the synaptic cleft in individual sections and summing over all sections.

Kainate, CNTF and quinolinate injections. *Cx30^{-/-}* mice were injected i.p. with kainic acid (30 mg/kg). Mice were monitored for 2 h after seizure onset. C57BL6 mice were injected with a lentivirus encoding ciliary neurotrophic factor (CNTF; 1 μl of a viral suspension at 100 ng p24 per μl ; ref. 47). One month later, these mice were injected with 0.5 μl of 80 mM quinolinate in the same striatum. After 7 d for kainic acid injections and 14 d for CNTF and quinolinate injections, mice were anesthetized, perfused and the brains processed for immunohistochemistry.

Electrophysiology. Acute transverse hippocampal slices (300–400 μm) were prepared as previously described²¹ from 8- to 25-d-old wild-type *Cx30^{+/+}* and *Cx30^{-/-}* mice³⁷ or, when mice were injected *in vivo* with lentiviruses, from 8-week-old mice. For all analyses, mice of both sexes and their littermates were used. Slices were maintained at room temperature in a storage chamber that was perfused with an artificial cerebrospinal fluid (ACSF) containing (in mM) 119

NaCl, 2.5 KCl, 2.5 CaCl₂, 1.3 MgSO₄, 1 NaH₂PO₄, 26.2 NaHCO₃ and 11 glucose, saturated with 95% O₂ and 5% CO₂, for at least 1 h before recording. Slices were transferred to a submerged recording chamber mounted on an Olympus BX51WI microscope equipped with infrared differential interference contrast microscopy and were perfused with ACSF at a rate of 1.5 ml/min at room temperature. All experiments were performed in the presence of picrotoxin (100 μM), and a cut was made between CA1 and CA3 to prevent the propagation of epileptiform activity, except when indicated. Extracellular field and whole-cell patch-clamp recordings were performed. Evoked postsynaptic or astrocytic responses were induced by stimulating Schaffer collaterals (0.1 Hz) in CA1 stratum radiatum with ACSF-filled glass pipettes. Stratum radiatum astrocytes were identified by their small cell bodies, low input resistance (~20 M Ω), high resting potentials (approximately –80 mV) and linear IV curves. Field excitatory postsynaptic potentials (fEPSPs) were recorded from 400- μm slices with glass pipettes (2–5 M Ω) filled with ACSF and placed in the stratum radiatum. Stimulus artifacts were blanked in sample traces. Somatic whole-cell recordings were obtained from visually identified CA1 pyramidal cells and astrocytes, using 5–10 M Ω glass pipettes filled with (in mM) 105 potassium gluconate, 30 KCl, 10 HEPES, 10 phosphocreatine, 4 Mg-ATP, 0.3 Tris-GTP, 0.3 EGTA (pH 7.4, 280 mOsm); or, for synaptic activity recordings (in mM), 115 CsMeSO₃, 20 CsCl, 10 HEPES, 2.5 MgCl₂, 4 Na₂-ATP, 0.4 Na-GTP, 10 sodium phosphocreatine, 0.6 EGTA, 0.1 spermine, 5 QX314 (pH 7.2, 280 mOsm); or, for astrocyte glutamate transporter current recordings (in mM), 130 KSCN, 20 HEPES, 10 EGTA, 1 MgCl₂, 2 Mg-ATP, 0.3 Na-GTP (pH 7.2, 280 mOsm). Glutamate transporter currents were evoked synaptically by stimulation of Schaffer collaterals and were recorded simultaneously with fEPSPs. The field recording pipette was placed 50 μm from the recorded astrocyte and transporter currents were blocked either by DL-threo- β -benzyloxyaspartic acid (TBOA, 200 μM) or by dihydrokainic acid DHK (100 μM) (approximately –50% of GLT current). Glutamate transporter whole-cell currents from astrocytes were also measured by local application of 10 mM D-aspartate for 1 s in the presence of 10 μM CPP and 0.5 μM tetrodotoxin (TTX). For intercellular coupling experiments, the internal solution contained biocytin (2 mg/ml) or sulforhodamine B (1 mg/ml), which diffused passively in astrocytes during 20 min in current-clamp mode. Intrinsic properties of CA1 pyramidal neurons were measured in current clamp in the presence of blockers of excitatory and inhibitory synaptic activity (10 μM 6-cyano-7-nitroquinoxaline-2,3-dione disodium (CNQX), 10 μM (RS)-3-(2-carboxypiperazin-4-yl)propyl-1-phosphonic acid (RS-CPP) and 100 μM picrotoxin). Evoked AMPAR-mediated EPSCs were measured at –70 mV, while NMDAR-mediated EPSCs were measured at +40 mV and a latency of 60 ms, when the AMPAR EPSC had fully decayed. Miniature excitatory postsynaptic currents (mEPSCs) were recorded at –70 mV in the presence of 0.5 μM TTX. Miniature inhibitory postsynaptic currents were recorded at –70 mV in the presence of 0.5 μM TTX and 10 μM CNQX. For field recordings, LTP was induced by tetanic stimulation of Schaffer collaterals (two trains of 100 Hz for 1 s, 20 s apart); for whole-cell recordings, LTP was induced by pairing at 2 Hz for 1 min with depolarization to 0 mV. AMPA-mediated whole-cell currents were obtained by local application of 10 μM (S)- α -amino-3-hydroxy-5-methyl-4-isoxazolepropionic acid (S-AMPA) for 5 s in the presence of 100 μM cyclothiazide and 0.5 μM TTX. Recordings were acquired with Axopatch-1D amplifiers (Molecular Devices, USA), digitized at 10 kHz, filtered at 2 kHz, and stored and analyzed on the computer using Pclamp9 and Clampfit9 software (Molecular Devices, USA). Picrotoxin, D-aspartate and biocytin were obtained from Sigma and all other chemicals were from Tocris.

Fear conditioning. Contextual fear memory is evaluated by returning the mice to an environment in which they were exposed to an electrical shock. Mice that have learned the association between the training environment and the electrical shock will exhibit increased freezing. To habituate the mice to the general procedures used during training and testing, adult male mice were placed in a transport cage and taken to the room housing the contextual fear conditioning apparatus, where they were handled. One day after the completion of handling, mice were trained. Experiments were performed in the early morning. Before fear conditioning, mice were preexposed for 5 min to both the training box (context A, 25 \times 25 \times 25 cm white plastic chamber) and control box (context B, 25 \times 25 \times 25 cm black plastic chamber). Behavior of the mice was observed with a CCD camera. One hour later, mice were placed in the training box. The mice were first left undisturbed for 2 min. Then they were presented with 5 unsignaled footshocks (1 s duration,

0.5 mA, randomly presented during 3 min period). Then the mice were placed 5 min in the control chamber. Mice were returned to their home cage. Long-term contextual fear memory was evaluated 24 h after conditioning. Mice were placed in the conditioning chamber and exposed to the context for 3 min, and then to the control chamber. Freezing time was measured during every minute of exposure to the context. Freezing was defined as lack of any visible movement except respiration, and it was monitored by visual inspection of the video images without knowledge of the genotype.

Computational model. We used Brownian dynamics implemented in MATLAB and C to simulate the motion of neurotransmitters in the synapse. The synaptic geometry was defined such that all its parts were rotationally symmetric and aligned to one single central axis of rotational symmetry (Fig. 5b). Two cylinders of infinite length and 700 nm diameter specified the pre- and postsynaptic terminal and were placed 20 nm apart to constitute the synaptic cleft, while a disk of 380 nm diameter defined the active zone (Fig. 5b).

The perisynaptic astroglial sheath was described as a cylindrical surface surrounding the synaptic cylinders placed at a distance of 20 nm from the edge of the synaptic terminals, corresponding to 180 nm from the edge of the active zone (Fig. 5b), as GLTs containing astrocytic processes are concentrated 100–200 nm from the edge of the active zone^{19,39}. At the synaptic cleft, a protrusion was raised from the glial sheath with a fixed height of 130 nm and with a depth varying between 0 and 150 nm (corresponding to distances between 180 and 30 nm to the active zone), as GLTs containing astrocytic processes are detected as close as 20 nm from the active zone^{19,39}. We maintained a distance of 20 nm between the glial protrusion surface and the pre- and postsynaptic cylinders by conically slanting the cylinders at the cleft (Fig. 5b). 100 AMPA receptors (AMPA) were placed on a round domain, which defined the postsynaptic density (PSD), with an area of $0.24 \mu\text{m}^2$ (corresponding to a disk of 560 nm diameter).

To model AMPAR dynamics, we used a kinetic scheme⁴⁸. Glial glutamate transporters (GLTs) were positioned on the glial sheath at a density of 5,000 GLTs per μm (refs. 2,16); however, only glial sheath within a distance of 250 nm to the middle plane of the synaptic cleft was covered with GLTs. Upon glutamate release, 3,000 glutamate molecules were located at a single point of release randomly chosen with uniform distribution on the cleft ceiling inside the active zone. Glutamate molecules diffused with a diffusion coefficient $0.2 \mu\text{m}^2/\text{ms}$ and could bind to transporters at a rate of $1.8 \times 10^7 \text{ M/s}$ (ref. 49).

We simulated glutamate association using the partial reflection method⁵⁰. The transporter current was computed as follows: the current is not proportional to the total number of bound glutamate molecules, but rather to the glutamate binding flux (i.e., the number of successful glutamate-to-transporter bindings per time), which is given by the derivative $dN(t)/dt$ of the concentration of the instantaneous number $N(t)$ of bound glutamate molecules. Similarly, the maximum amplitude of the AMPAR current is proportional to the number of open AMPARs. As we only consider amplitude ratios, proportionality constants are not needed. All currents were sampled for 4 ms at a fixed time step size of $0.5 \mu\text{s}$ and were averaged over 600 runs. As glutamate dissociation from transporters takes place at times much longer than 4 ms, glutamate unbinding was neglected.

Statistics. Prior statistical comparison, normality test as well as variance analysis were performed and the appropriate two-sided statistical parametric or nonparametric test was used. Two-tailed unpaired or paired *t* tests were used for between-group comparisons. Statistical significance for within-group comparisons was determined by one-way or two-way ANOVAs followed by *post hoc* tests. The Kolmogorov-Smirnov test was used for cumulative distribution comparison. Appropriate sample sizes were based on best practices in the literature as well as on ethical standards to minimize numbers of animals for experiments, and were dictated by the magnitude of experiment-to-experiment variation. All statistical analysis was performed in GraphPad Prism (GraphPad Software, USA) and Statistica (StatSoft, USA). There was no explicit blinding or randomization except for behavioral tests, as indicated in the fear conditioning section.

47. Escartin, C. *et al.* Ciliary neurotrophic factor activates astrocytes, redistributes their glutamate transporters GLAST and GLT-1 to raft microdomains, and improves glutamate handling in vivo. *J. Neurosci.* **26**, 5978–5989 (2006).
48. Jonas, P., Major, G. & Sakmann, B. Quantal components of unitary EPSCs at the mossy fibre synapse on CA3 pyramidal cells of rat hippocampus. *J. Physiol. (Lond.)* **472**, 615–663 (1993).
49. Geiger, J.R.P., Roth, A., Taskin, B. & Jonas, P. Glutamate-mediated synaptic excitation of cortical interneurons. in *Ionotropic Glutamate Receptors in the CNS: Handbook of Experimental Pharmacology* (eds. Jonas P. & Monyer H.) 363–398 (Springer, Berlin, 1999).
50. Singer, A., Schuss, Z. & Holcman, D. Narrow escape and leakage of Brownian particles. *Phys. Rev. E* **78**, 051111 (2008).